NEW CONSTRAINTS ON THE TIMING, RATE, AND STYLE OF EXHUMATION OF THE WOOD HILLS AND PEQUOP MOUNTAINS, ELKO COUNTRY, NEVADA

FRANKLIN D. WOLFE (2016)
B.S. CANIDATE: HONORS THESIS
ADVISOR: DR. JEFFREY M. RAHL
WASHINGTON AND LEE UNIVERSITY
DEPARTMENT OF GEOLOGY

TABLE OF CONTENTS

ABSTRACT **5**
INTRODUCTION **6**
GEOLOGIC SETTING 15
METAMORPHIC CORE COMPLEX 26
(U-TH)/HE THERMOCHRONOLOGY 29
METHODS **32**
FIELD WORK 32
MINERAL SEPARATION 34
ZIRCON GRAIN SELECTION & (U-TH)/HE ANALYSIS 35
RESULTS **37**
DISCUSSION **42**
TIMING OF THE ONSET OF EXTENTION ON RUBY MOUNTAIN DETACHMENT FAULT 42
RATE OF EXHUMATION ON THE RUBY MOUNTAIN DETACHMENT FAULT 48
RECONNAISSANCE ANALYSIS OF THE PEQUOP MOUNTAINS 52
SAMPLE JR_D 55
CONCLUSIONS **56**
ACKNOWLEDGEMENTS **57**
WORKS CITED **58**
APPENDIX A – FULL DATA TABLE **65**
APPENDIX B – METHODS & DATA EXPLANATION **67**
(U-TH)/HE METHODS 67
(U-TH)/HE DATA EXPLANATION 68

LIST OF FIGURES AND TABLES

FIGURE 1: STUDY AREA DIGITAL PHOTOS....**6**
FIGURE 2: SPATIAL EXTENT OF METAMORPHIC CORE COMPLEXES **8**
FIGURE 3: EVOLUTION OF A METAMORPHIC CORE COMPLEX **9**
FIGURE 4: STUDY AREA SPATIAL EXTENT **11**
FIGURE 5: GEOMORPHOLOGY AND TOPOGRAPHY OF STUDY AREA **12**
FIGURE 6: RM-EHR FOOTWALL DISECTION....**13**
FIGURE 7: TECTONIC EVOLUTION AND DOCUMENTED AGES OF EXHUMATION ..**14**
FIGURE 8: EXTENSIONAL PROVINCES MAP....**17**
FIGURE 9: TECTONIC MAP OF NEVADA **18**
FIGURE 10: METAMORPHIC MAP OF THE STUDY AREA **20**
FIGURE 11: SOUTHERN RUBY MOUNTAINS TECTONIC HISTORY **21**
FIGURE 12: METAMORPHIC MAP OF THE PEQUOP MOUNTAINS....**23**
FIGURE 13: TEMPERATURE ESTIMATES OF THE PEQUOP MOUNTAINS **24**
FIGURE 14: METAMORPHIC MAP OF THE WOOD HILLS....**25**
FIGURE 15: SHEAR ZONE DIAGRAM....**28**
FIGURE 16: CLOSURE TEMPERATURES FOR THERMOCHRONOMETERS....**30**
FIGURE 17: ZIRCON (U-TH)/HE SYSTEM SIMPLIFIED VERSION....**31**
FIGURE 18: SAMPLE COLLECTION SITES **33**
FIGURE 19: MINERAL SEPARATION IMAGES **34**
FIGURE 20: GRAIN SELECTION IMAGES....**35**
FIGURE 21: ZIRCON (U-TH)/HE ANALYSIS IMAGES....**36**
FIGURE 22: PEQUOP MOUNTAIN AGES....**39**
FIGURE 23: WOOD HILLS AGES **39**
FIGURE 24: CLOVER HILL....**41**
FIGURE 25: CONCEPTUAL MODEL OF FOOTWALL EXHUMATION....**44**
FIGURE 26: A-A’ WOOD HILLS TRANSECT....**45**
FIGURE 27: JR_O MYLONITIC FABRIC....**46**
FIGURE 28: INCORPORATING AGES FROM GIFFORD ET AL. (2008) **49**
FIGURE 29: INCORPORATING TEMPERATURE ESTIMATES FROM HOWLAND....**53**

FIGURE 30: PROPOSED CHRONTOURS FOR THE WOOD HILLS.....**47**

TABLE 1A: ABBREVIATED RESULTS TABLE **38**
TABLE 1: FULL RESULTS TABLE **65**

ABSTRACT

In this study, zircon (U-Th)/He analysis is used to documents the timing, rate, and style of exhumation of the Wood Hills and Pequop Mountains, which are part of the Ruby Mountains-East Humboldt Range metamorphic core complex. This is a premier natural laboratory in the Basin and Range Province for studying the dynamics of metamorphic core complexes, because it exposes middle to lower crustal rocks (~30 km deep) and the kinematics of exhumation are well-constrained in a mylonitic shear zone on the western extent of the complex. What makes this complex unique is that the footwall was dissected by later high-angle normal faults, which have preserved the higher structural levels of the complex at their current position (Wood Hills and Pequop Mountains) and exposed the deeper levels beneath the mylonitic zone (East Humbolt Range). Great debate has emerged over the timing of on-set of exhumation of the core complex along the Ruby Mountain Detachment Fault. Some argue that it began during Miocene or younger times, which is consistent for the dominant phase of extension throughout the Basin and Range, whereas, others believe it began during earlier times (Oligocene to Eocene). Results from this study reveal that slip along the Ruby Mountain Detachment Fault must have begun by Oligocene, but probably Eocene times. The trend in younging of apparent $^{40}Ar/^{39}Ar$ muscovite, biotite, and hornblende ages towards the NW, which has been documented for the Southern Ruby Mountains by Colgan et al. (2010) and the East Humboldt Range by McGrew and Snee (1994), is consistent with the findings presented here for the Wood Hills and Pequop Mountains. Lastly, the Pequop Mountains reached temperatures (depths) high enough to reset zircon (U-Th)/He thermochronometers; however, inconclusive evidence is found to confidently declare that the exhumation of these mountains is due to slip along the Ruby Mountain Detachment Fault.

INTRODUCTION

A prominent physiographic feature of the western North American topography is north to south trending of mountain ranges and adjacent flat basins, which constitute the Basin and Range Province (Figure 1). This topography has been interpreted as the result of a large amount of east-to-west extension that began during early Cenozoic times and has continued into the present, though a complex interrelation of extension, volcanism, and plate boundary tectonics (Sonder and Jones, 1999). The forces responsible for driving the bulk of the activity are thought to be basal normal forces or from buoyancy internal to the crust and lithospheric mantle (with a smaller influence from basal traction) (Sonder and Jones, 1999). These crustal buoyancy forces combined with a divergent tectonic boundary between ~28-16 Ma drove extension in the Southern Basin and Range. In the northern Basin and Range Province, extension is estimated to be as high as 300% (Bogen and Schweickert, 1985).

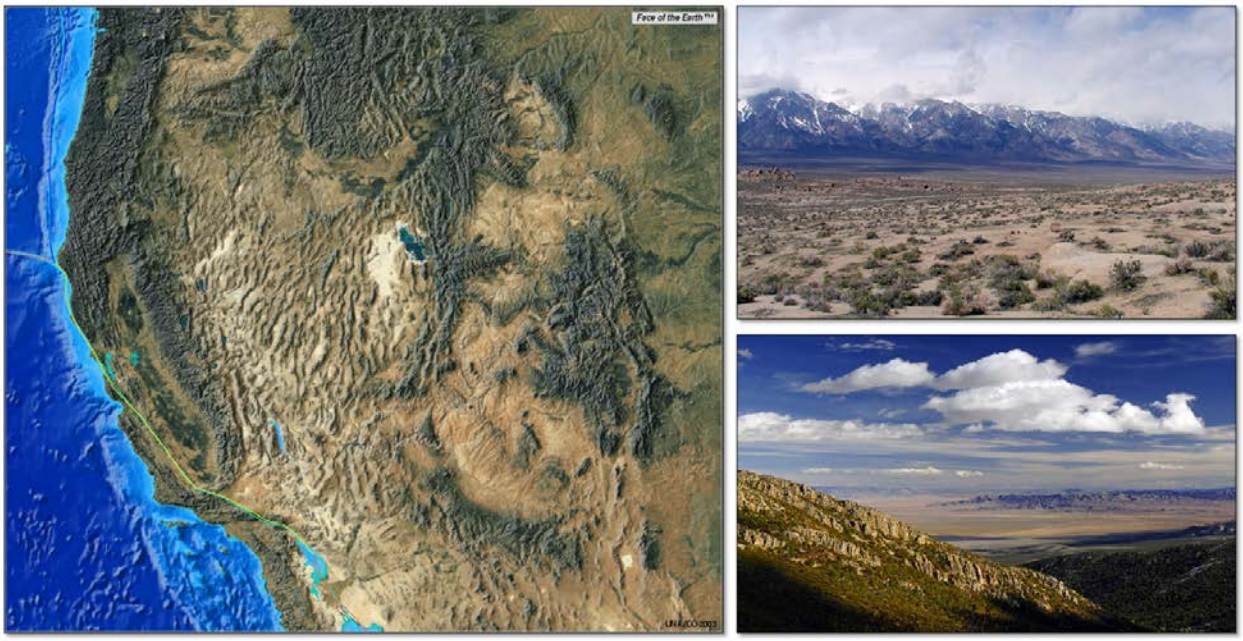

Figure 1. Views of the study area demonstrating the north to south trending of mountain ranges with adjacent low-lying, flat plains – typical of the Basin and Range Province.

The magnitude of extension and the direction of tectonic transport are variable throughout the Basin and Range Province. Additionally, extension rates are strongly variable spatially and temporally across the broader extensional province, and it is difficult to accurately reconstruct the strain history of a region because it requires knowledge of both extension rate and width of an extending region as a function of time (Sonder and Jones, 1999). In the Central Basin and Range Province, early extension rates were more than 20 mm/a during ~8-16 Ma (Sonder and Jones, 1999). More poorly constrained estimates for the Northern Basin and Range Province give estimates of ~4-9 mm/a since ~35-45 Ma (Sonder and Jones, 1999). In the Southern Basin and Range Province, Spencer and Reynolds (1991) estimated average extension rates of ~8-9 mm/a from ~25-15 Ma.

Where local extension is the greatest, mid-lower crustal rocks have been exhumed to the surface forming metamorphic core complexes (Figure 2). Metamorphic core complexes develop when upper crustal blocks slide off lower crustal blocks along mylonitic shear zones, allowing lower crustal rocks to isostatically rise towards the surface (see Metamorphic Core Complex section below for further detail) (Figure 3).

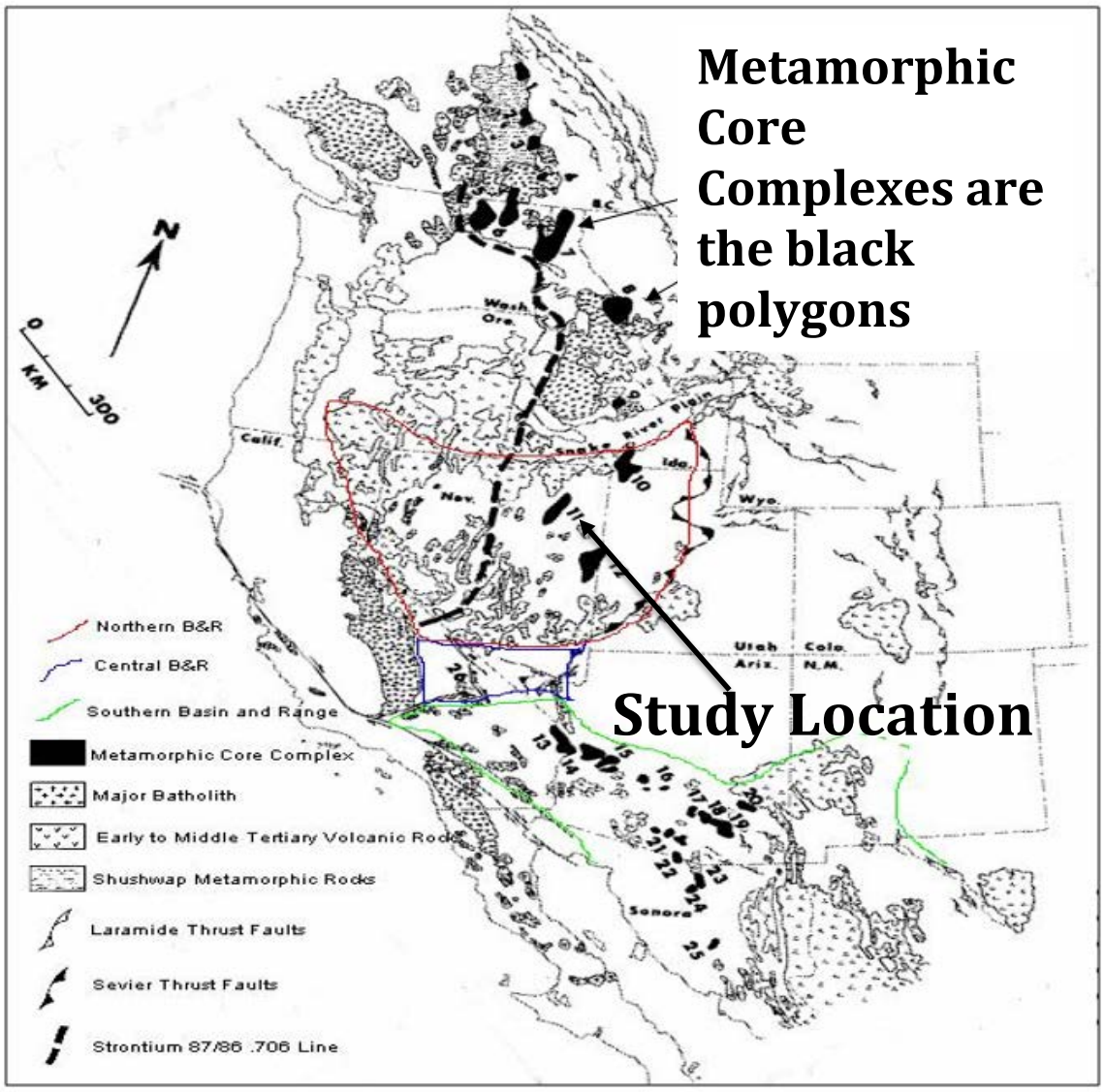

Figure 2. Spatial extent of metamorphic core complexes within the Basin and Range Province. (adapted from Davis and Reynolds 1986)

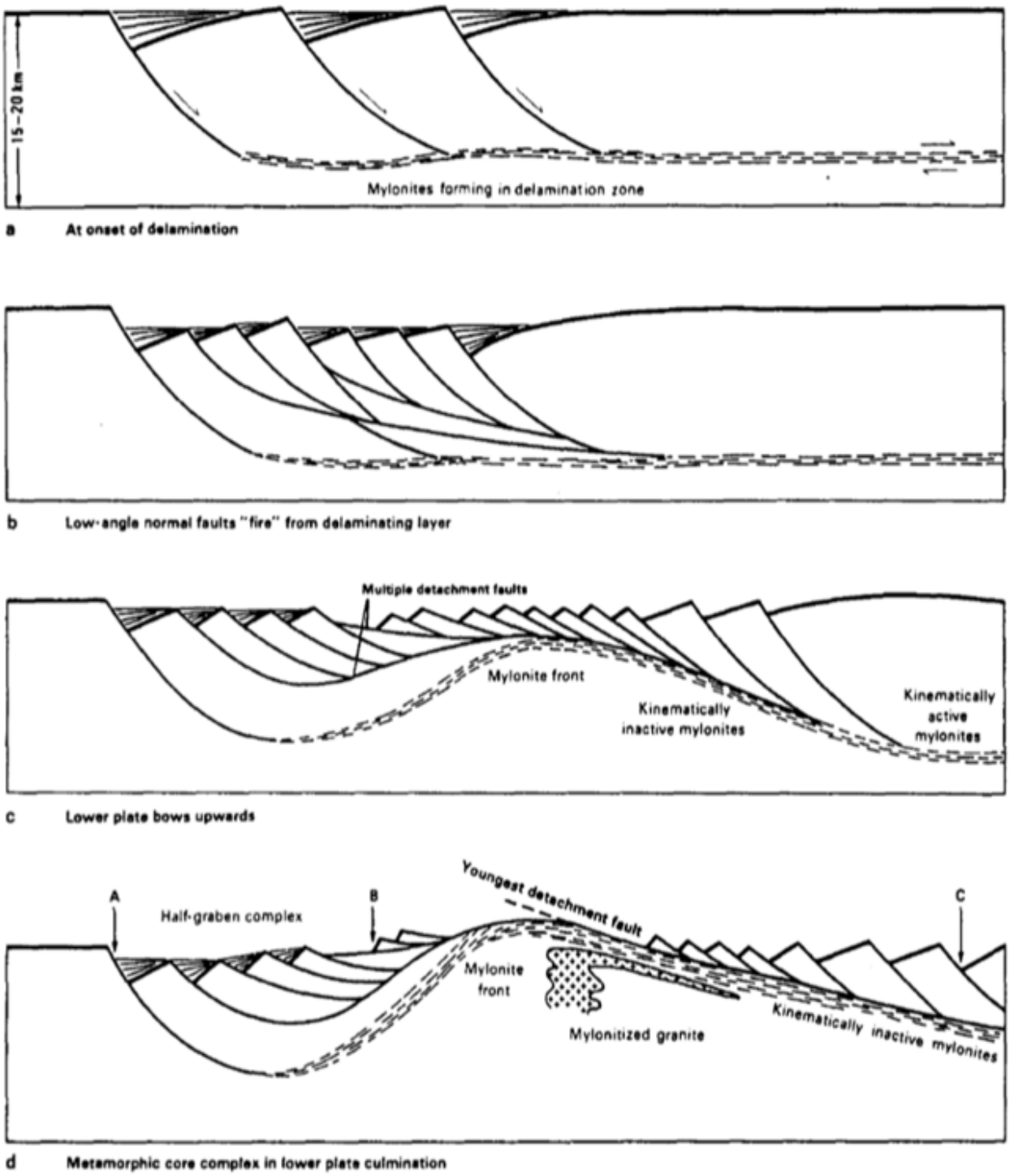

Figure 3. The formational evolution of a metamorphic core complex. (from Lister and Davis 1989)

The timing of extension throughout the Basin and Range Province is suspected to be dominantly Miocene or younger in age; however, much later extension (Oligocene to Eocene and older) has been documented in specific areas (Sonder and Jones, 1999; Wernicke and Snow, 1998). In many local areas within the Basin and Range Province, the timing of extension is poorly constrained. This study is focused on the Ruby Mountain-East Humboldt Range Metamorphic Core Complex, which is located in northeastern Nevada adjacent to Wells, Nevada (Figures 2 & 4).

The Ruby Mountain Detachment Fault is a regionally significant structure responsible for exhumation of the Ruby Mountains-East Humboldt Range metamorphic core complex. Despite numerous thermochronometric studies, many uncertainties remain concerning the rate, style, and timing of the on-set of extension along the Ruby Mountain Detachment Fault. Some believe that the bulk of regional extension occurred during the middle-to-late Miocene, which is consistent with the dominant phase of exhumation for the Basin and Range Province (Colgan et al., 2010; Snee et al., 2016). Colgan et al. (2010) sites rapid unroofing of the Harris Pass pluton in two distinct Miocene events (~16-17 Ma and 10-12 Ma) and a lack of significant sedimentation before the deposition of the Humboldt Formation in Huntington and Lamoille Valleys (~16-10 Ma) as evidence that significant slip on the Ruby Mountain Detachment Fault was mainly mid-Miocene or younger. Others argue that extension began as early as the Eocene, which has been documented for specific areas throughout the Basin and Range Province (McGrew and Snee, 1994). McGrew and Snee (1994) used $^{40}Ar/^{39}Ar$ biotite cooling ages and a suite of WNW-deformed 29 Ma biotite monzogranitic orthogneisses in the East Humboldt Range to argue for progressive unroofing of the footwall of a WNW-rooting crustal scale normal fault system between ~30 Ma and 21 Ma (McGrew and Snee, 1994; McGrew and Casey, 1998) (Figure 7).

But, the data from McGrew and Snee (1994) are limited and equivocal, and some have argued that the $^{40}Ar/^{39}Ar$ ages may represent a tilted partial retention zone, which assumed its position during Mesozoic contraction (Colgan, 2010). For example, Colgan et al. (2010) attributes published Oligocene to early Miocene K-Ar biotite and zircon fission track dates from the Harrison Pass Pluton (Southern Ruby Mountains) to be partially reset, rather than directly recording fault slip. The goal of this study is to use zircon (U-Th)/He thermochronometry to provide new constraints on the timing, rate, and style of exhumation of the Wood Hills and Pequop Mountains (located east of the Wood Hills), which are part of the Ruby Mountains-East Humboldt Range metamorphic core complex.

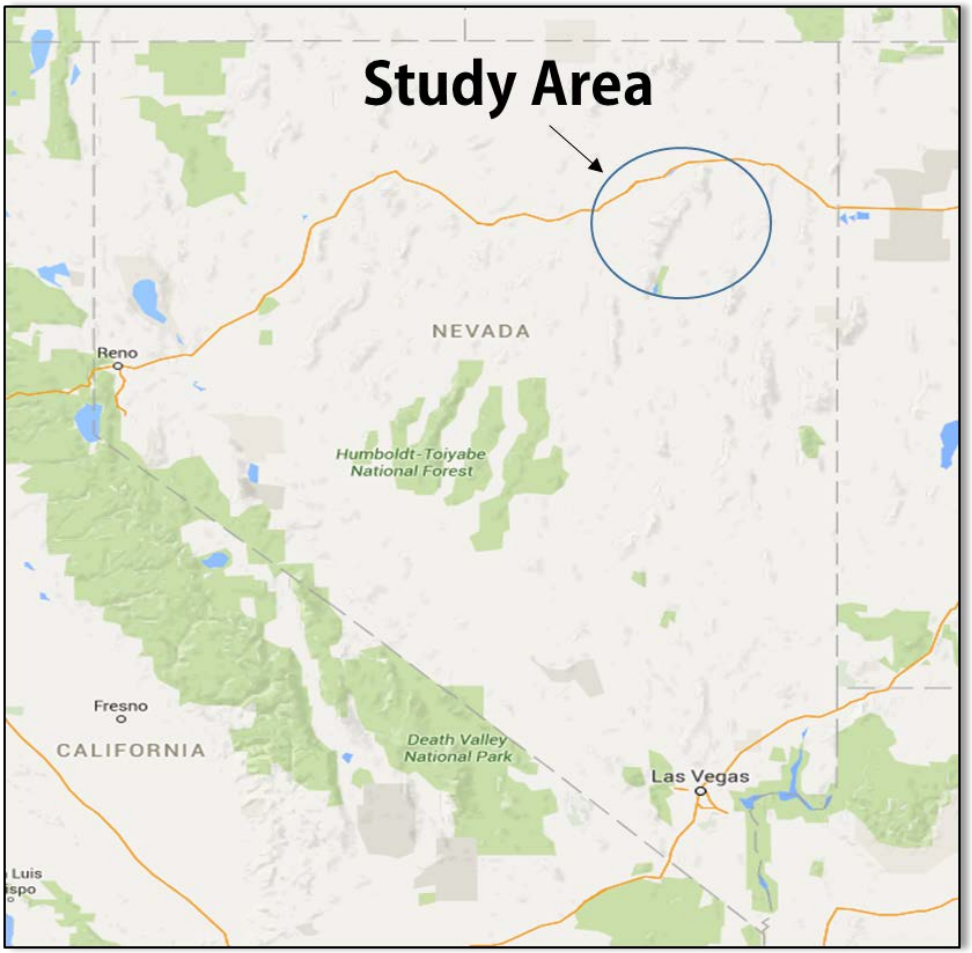

Figure 4. Spatial extent of the study area.

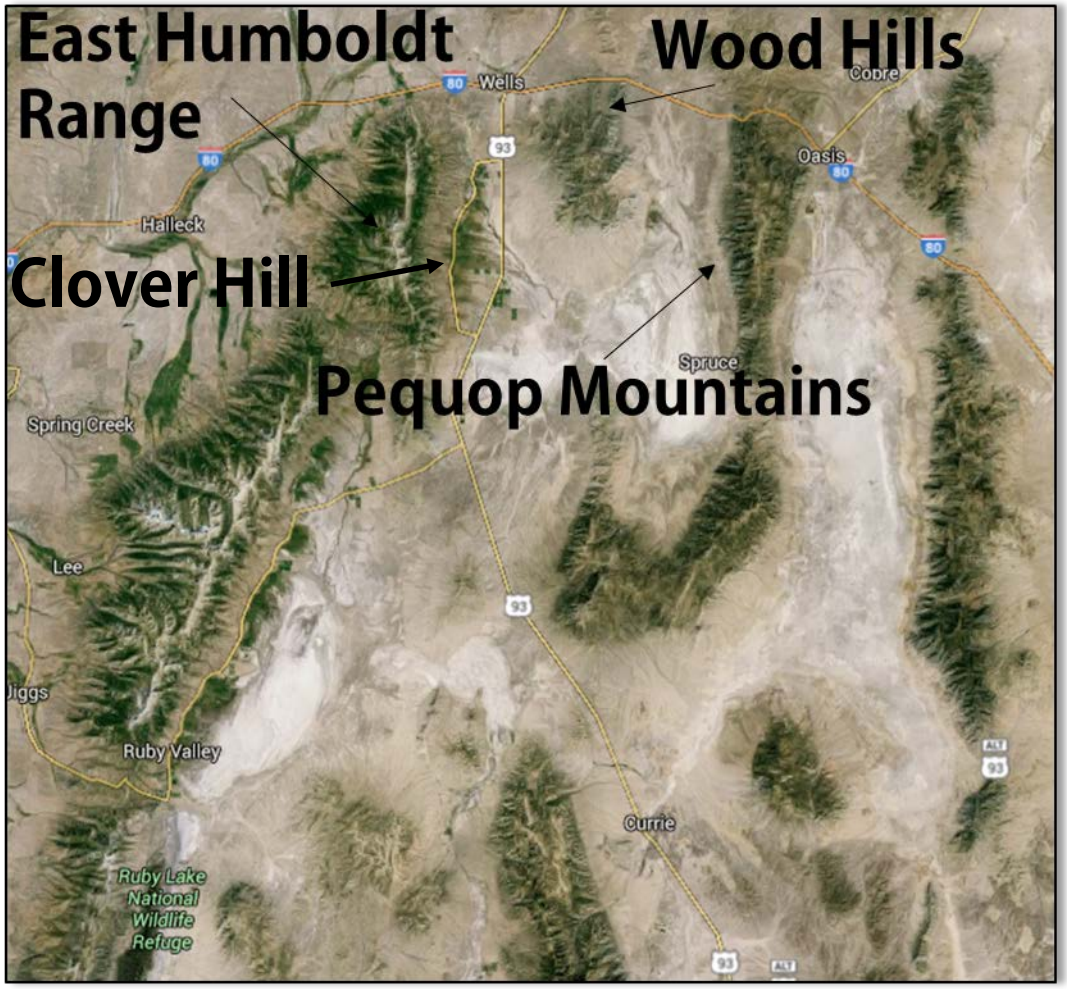

Figure 5. Geomorphology of the study area. North to south trending mountain ranges and low-lying, flat plains, typical of the broader Basin and Range Province.

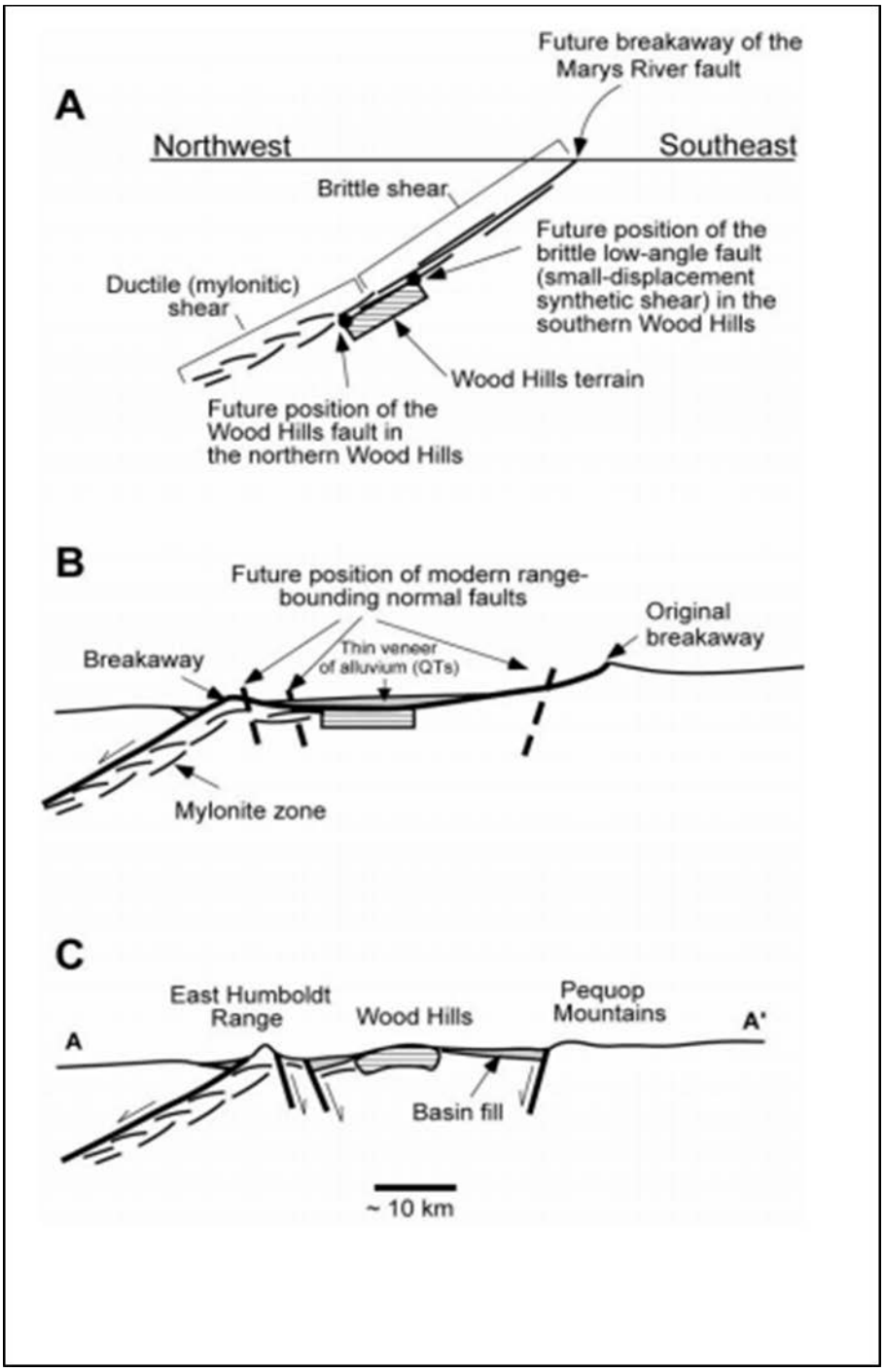

Figure 6. The evolution of the footwall of the Ruby Mountains-East Humboldt Range Metamorphic Core Complex. A shows the footwall prior to later normal faulting. B demonstrates the effects of normal faulting. C shows the current locations of the upper structural levels of the footwall – the Wood Hills and Pequop Mountains. (from Camilleri and Chamberlin 1997)

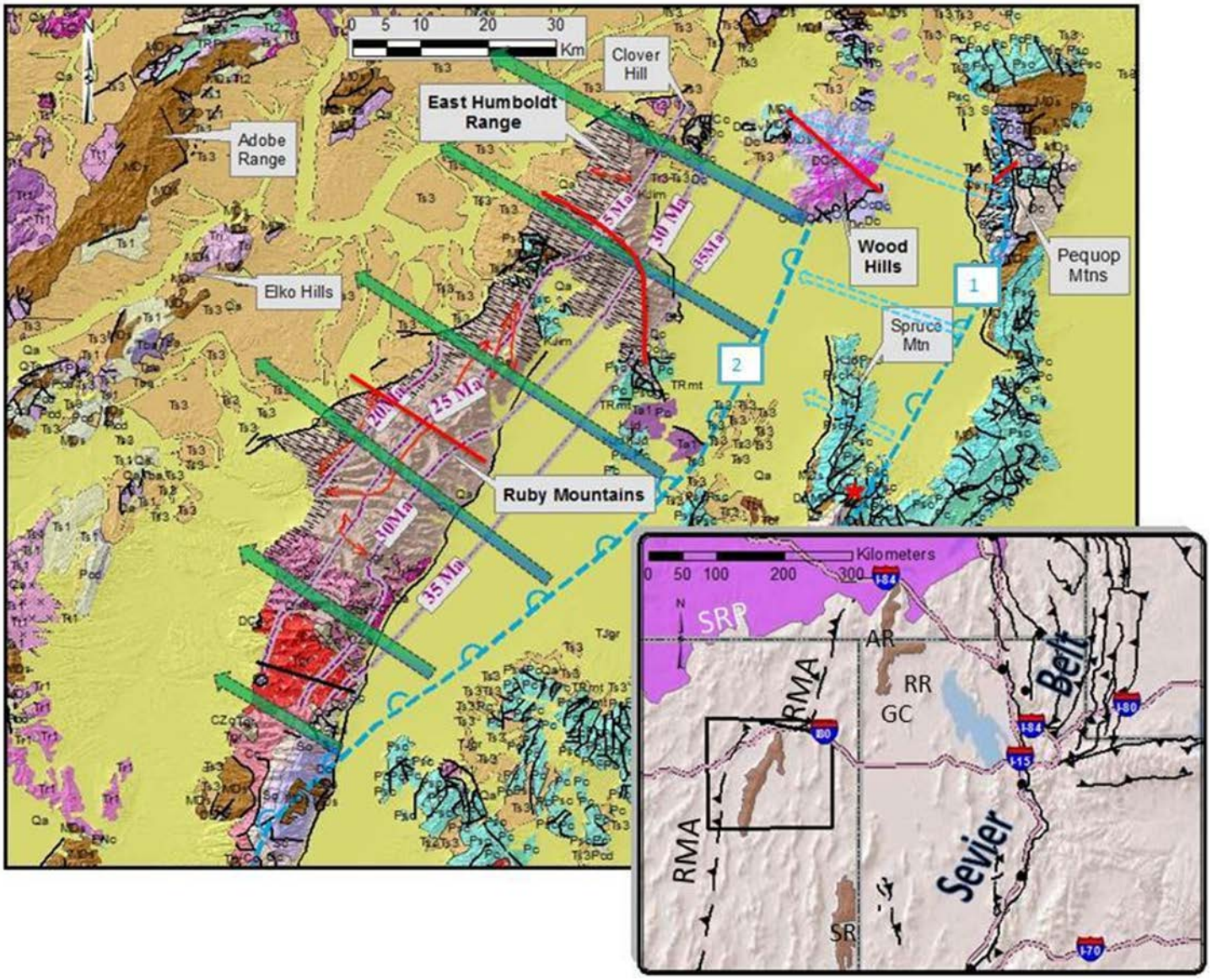

Figure 7. McGrew and Snee (1994) document northwest younging from $^{40}Ar/^{39}Ar$ biotite cooling ages and a suite of WNW-deformed 29 Ma biotite monzogranitic orthogneisses in the East Humboldt Range. Chrontours of equal exhumation age are demonstrated with magenta lines. Green arrows demonstrate the direction of tectonic transport. (from McGrew and Snee (1994))

Geologic Setting

In comparison to other tectonically similar areas, such as the Aegean Sea and the North Sea, the Basin and Range Province provides an excellent laboratory for studying metamorphic core complex interactions due to its climate (lack of vegetation) and high altitude, which preserves great outcrop quality (Sonder and Jones, 1999).

The Ruby Mountains-East Humboldt Range metamorphic core complex is located within the hinterland region of the Sevier Orogen (Howard, 2003). This complex is a great laboratory for the study of core complex development in the region because it has exhumed rocks up to ~30 km deep (750°C & 0.8 GPa) and preserves kinematic indicators for exhumation on its western margin along a mylonitic shear zone (SE to NW). Geomorphologically, this region is characterized by north to south trending mountain ranges and adjacent low-lying, flat plateaus, similar to the rest of the Basin and Range Province (Figure 5). It is unique because later, high-angle normal faults dissected the higher structural levels (Wood Hills and Pequop Mountains) to their current positions in the field, and also exposed the deeper levels below the mylonitic shear zone (East Humboldt Range) (Figure 6).

The Ruby Mountains-East Humboldt Range metamorphic core complex exposes Precambrian basement, Neoproterozoic-Paleozoic metamorphosed shelf margin sediments, and Mesozoic-Cenozoic plutonic rocks (Snee et al., 2016). These sediments began accumulating on a Late Pre-Cambrian passive margin setting that persisted through the Triassic.

During the late Mesozoic and early Tertiary, the entire edge of western North America was a convergent plate boundary as the Farallon plate was subducted (Sonder and Jones, 1999). Strata were duplicated across the study area during Mesozoic crustal shortening in the Sevier Orogeny, with the foreland to the east, and the same stratigraphic units are exposed in the East

Humboldt Range, Wood Hills, and Pequop Mountains. This phase of contraction led to significant crustal thickening (~60-80 km thick). The growing consensus is that this led to the formation of a regionally high elevation plateau, known as the Nevadaplano Plateau, in the hinterland of the Sevier orogenic belt during the Late Cretaceous (DeCelles, 2004; Henry, 2009; Snell et al., 2014).

In the western-most area of the study area in the Ruby Mountains-East Humboldt Range, Dilles (Keck 2016) confirmed the age of peak metamorphism to be in the late Cretaceous during prograde burial ~80 Ma through U-Pb zircon analysis. The plateau was given its name because it is interpreted and inferred to be similar to the present-day Andean Altiplano plateau (Long et al., 2015). In the Southern Ruby Mountains, mesoscopic and microscopic analysis of the granitic rocks in the 500 meter thick shear zone with kinematic indicators suggesting top-to-the-south shear associated with regional compression, thickening, and thrusting and high-grade metamorphism reaching 750-800 °C / 0.7-1.1 GPa (Sousa, 2008).

Cenozoic extension, which has exposed rocks form various levels within the 'Nevadaplano', occurred over a wide area of Western America, from as far north as Canada to as far south as Mexico, and east from California to Utah, Montana and New Mexico (Sonders and Jones, 1999). The extended area can be subdided into four distinct regions: (1) the Omineca in Washington and British Columbia; (2) the Rocky Mountains Basin and Range in Montana, Idaho, and Wyoming; (3) the Basin and Range in Nevada, Utah, Arizona, California, and northern Mexico; (4) and the Rio Grande Rift, which merges at its southern end with the Basin and Range (Sonder and Jones, 1999). The study here will focus on (3) the Basin and Range.

The Basin and Range Province can be subdivided into the Northern, Central, and Southern Basin and Range (Figure 8). The Northern Basin and Range has the highest average

elevation, highest heat flow, and thinnest crust (Sonders and Jones, 1999). The Southern Basin and Range has the lowest average elevation, lowest heat flow, and is tectonically least active. The Central Basin and Range represents a transition zone between the two (Sonders and Jones, 1999).

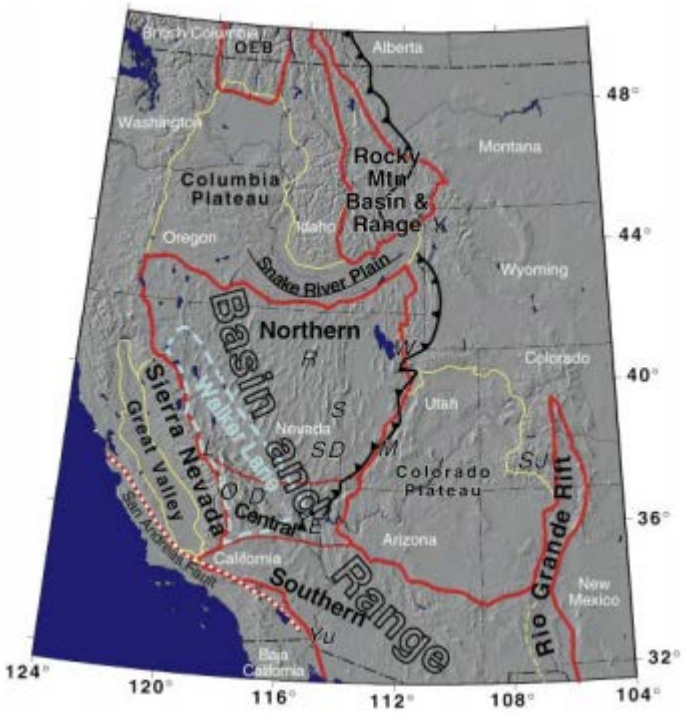

Figure 8. Map demonstrating the spatial extent of the extensional provinces in western North America. (from Sanders and Jones (1999))

Extension not associated with the Mesozoic contractional event is likely to have initiated earliest in the north in the Omineca extensional belt and the Rocky Mountain Basin and Range in Eocene times (~55-45 Ma) and extended as far south as the Ruby Mountains (Sonders and Jones, 1999). A north-to-south migration of volcanism, which has been well-documented across the Northern Basin and Range from ~40-20 Ma is coincident with large-scale extension and sedimentation though most of the eastern two-thirds of the Northern Basin and Range by late

Paleogene time (Sonders and Jones, 1999). Extension in the Southern Basin and Range began ~25 Ma and appears to have migrated northward with time (Sonders and Jones, 1999). It is difficult to estimate the magnitude of extension in the Southern Basin and Range because the San Andreas Fault now cuts through the westernmost portions, but a transect across most of the range contains 80-90 km of extension (Spencer & Reynolds, 1991). The latest initiation of extension occurred in the Central Basin and Range ~16-14 Ma (Sonders and Jones, 1999). Total extension in the Central Basin and Range has been estimated to be 250 ± 50 km (Wernicke et al., 1988). Total extension in the Northern Basin and Range is suspected to be comparable to the Central Basin and Range.

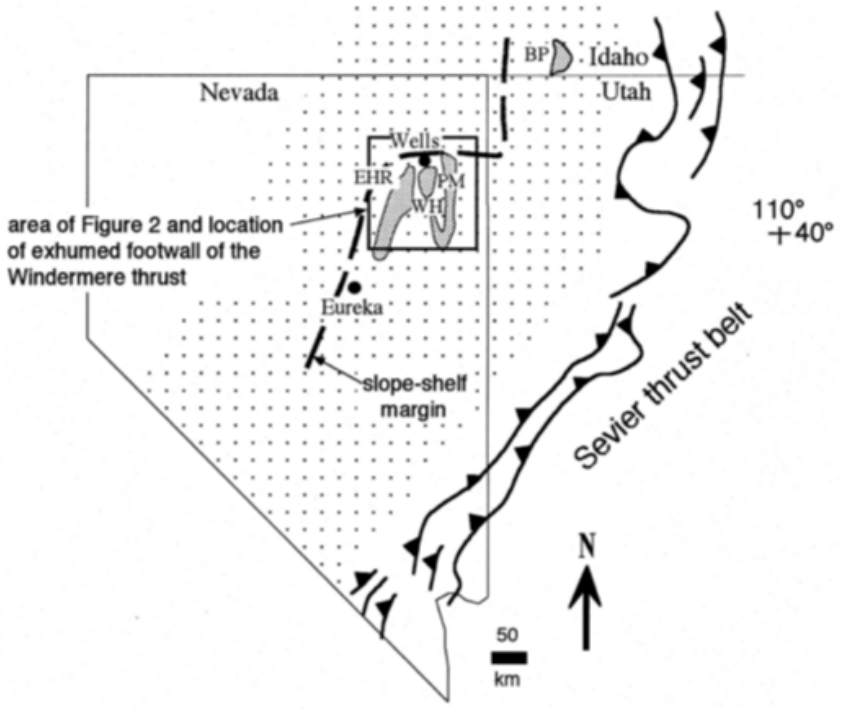

Figure 9. Tectonic map of Nevada and western Utah showing the position of the Sevier fold and thrust front, its hinterland (strippled region), and the location of the area of study, EHR = East Humboldt Range; WH = Wood Hills; PM = Pequop Mountains. Position of the slope-shelf margin is after Miller et al. (1991). (from Camilleri 1998)

In our study area, the timing of the onset of late Cenozoic extension along the Ruby Mountain Detachment Fault exhumed these middle to lower crustal rocks towards the surface remained poorly constrained. The WNW kinematics of the detachment fault are well-known from meso- and microscale kinematic indicators preserved in the mylonitic shear zone exposed along the western side of the Ruby Mountains (Figure 10) (Camilleri, 1998; MacCready et al., 1997). Additionally, thermochronometric studies completed in this area have documented younging towards the northwest in the direction of tectonic transport as would be expected for exhumation along a detachment fault in the northern and southern ranges (Stockli, 2005; Reiners, 2005; McGrew and Snee, 1994; Colgan et al., 2010) (see Figure 7 above for north; Figure 10 demonstrates initiation of mylonitic shear zone in the Southern Ruby Mountains ~16-12 Ma). Tertiary high-angle normal faulting from the Mary's River Fault System has exposed these rocks at the surface, creating an extraordinary natural laboratory for studying metamorphic core complex exhumation. The high-angle normal faults have dissected footwall of the detachment fault, dropping higher structural levels, the Wood Hills and Pequop Mountains, to their present day position to the east of the East Humboldt Range (See Figure 6 shown previously). Due to this relationship, this area provides a unique opportunity to examine the entire footwall of the Ruby Mountain Detachment Fault from the highest structural levels to rocks as deep as the mylonitic shear zone. Metamorphic grade increases northwestward across the study area (Camilleri, 1998) (Figure 10).

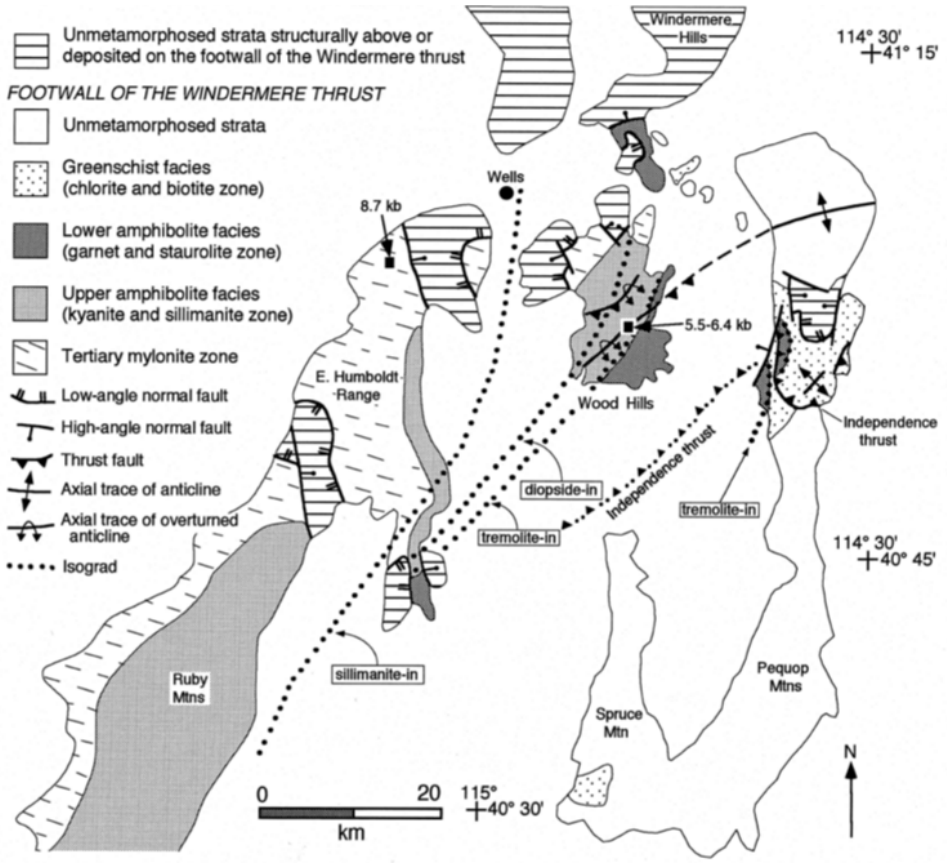

Figure 10. Simplified tectonic and metamorphic map of the Pequop Mountains, Wood Hills, Ruby Mountains, and East Humboldt Range. (from Camilleri 1998)

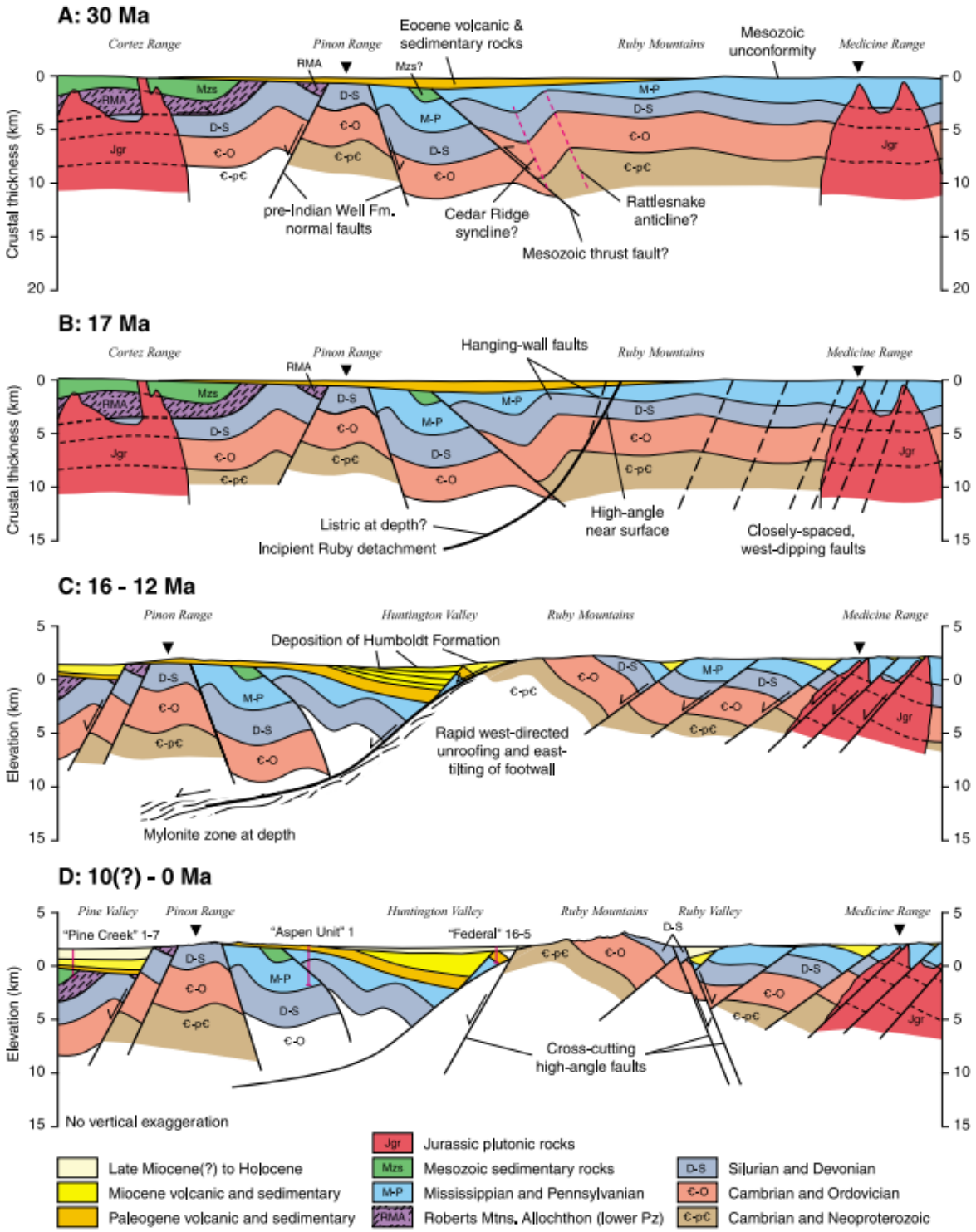

Figure 11. Eocene to present-day tectonic history of the southern Ruby Mountains and nearby ranges in the southern extent of the metamorphic core complex. (from Colgan et al. 2010)

The Pequop Mountains are located farthest east and preserve the lowest grade of metamorphism (unmetamorphosed to lower amphibolite facies) (Camilleri, 2010). The gently eastward dipping top-west normal fault, the Pequop Fault (~84-41 Ma), separates the Pequop Mountains into two domains of Proterozoic-Paleozoic rocks. The two domains have different structural and metamorphic characteristics, which increase in metamorphic grade with burial depth (Camilleri, 2010) (Figure 12). The Protersozoic-Paleozoic rocks in the footwall of the Pequop fault range from unmetamorphosed to lower amphibolite facies and metamorphic grade increases with stratigraphic depth (Camilleri, 2010). The hanging wall of the fault consists of unmetamorphosed east-dipping sequence of Ordovician to Mississippian strata that were overthrust over east-dipping Permian strata (Camilleri, 2010). Camilleri and Chamberlain (1997) bracket the age of the Pequop Mountain metamorphism (age of crustal shortening) between 154 and 86 Ma. They did this by dating a pre-metamorphic dike that is deformed by the metamorphic fabric (older bracket) and a U-Pb metamorphic titanite from the Toano Limestone, which is inferred to represent the time of peak metamorphism (younger bracket). Paleozoic strata within the hanging wall of the fault to the east are unmetamorphosed. Calcite-dolomite exchange thermometry shows that carbonates in the Pequops preserve peak metamorphic temperatures that increase from ~300-500 °C towards the south and with increased structural depth within the footwall (Howland, Keck 2016) (Figure 13).

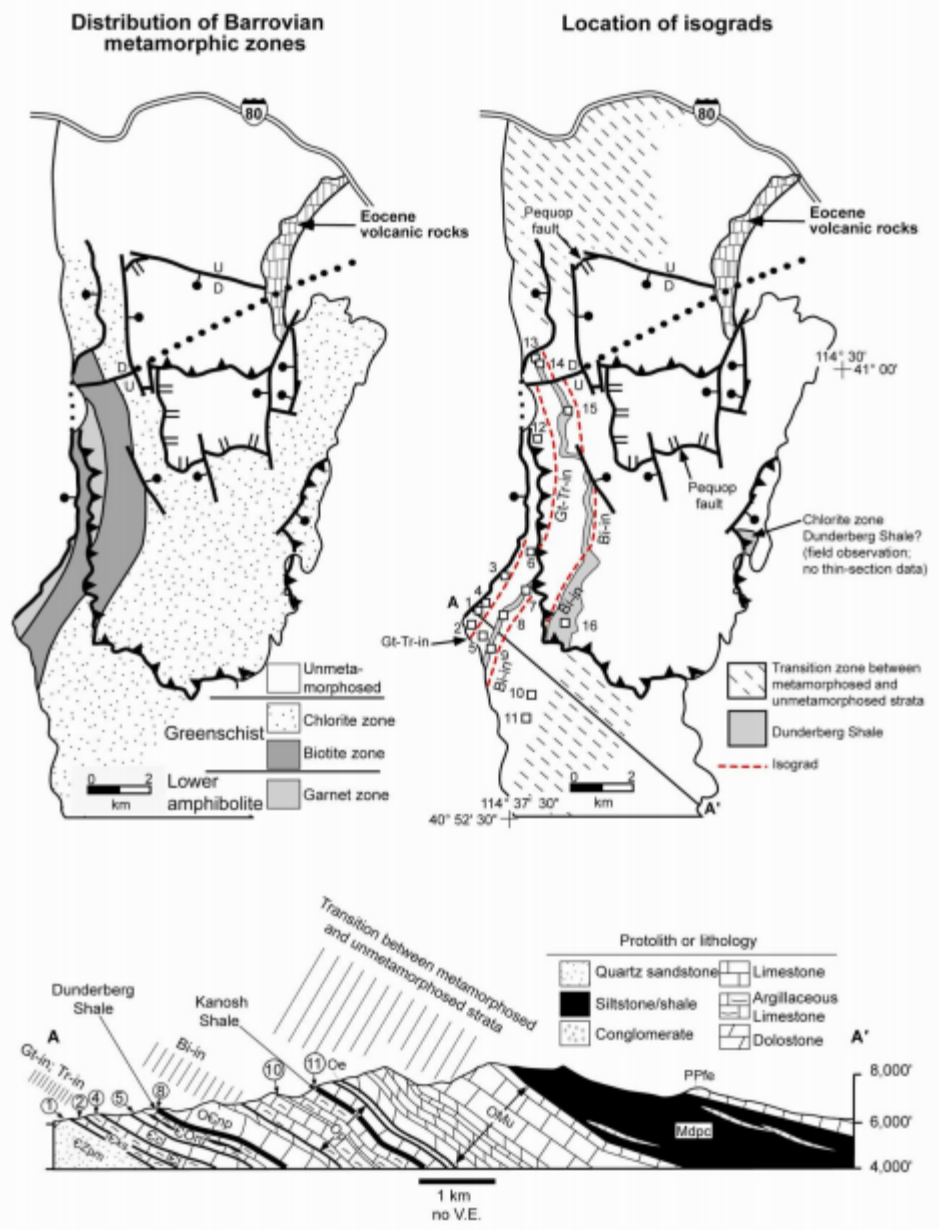

Figure 12. Metamorphic maps and cross section of the Pequop Mountains. The cross section is modified after Camilleri and Chamberlin (1997). (from Camilleri 2010)

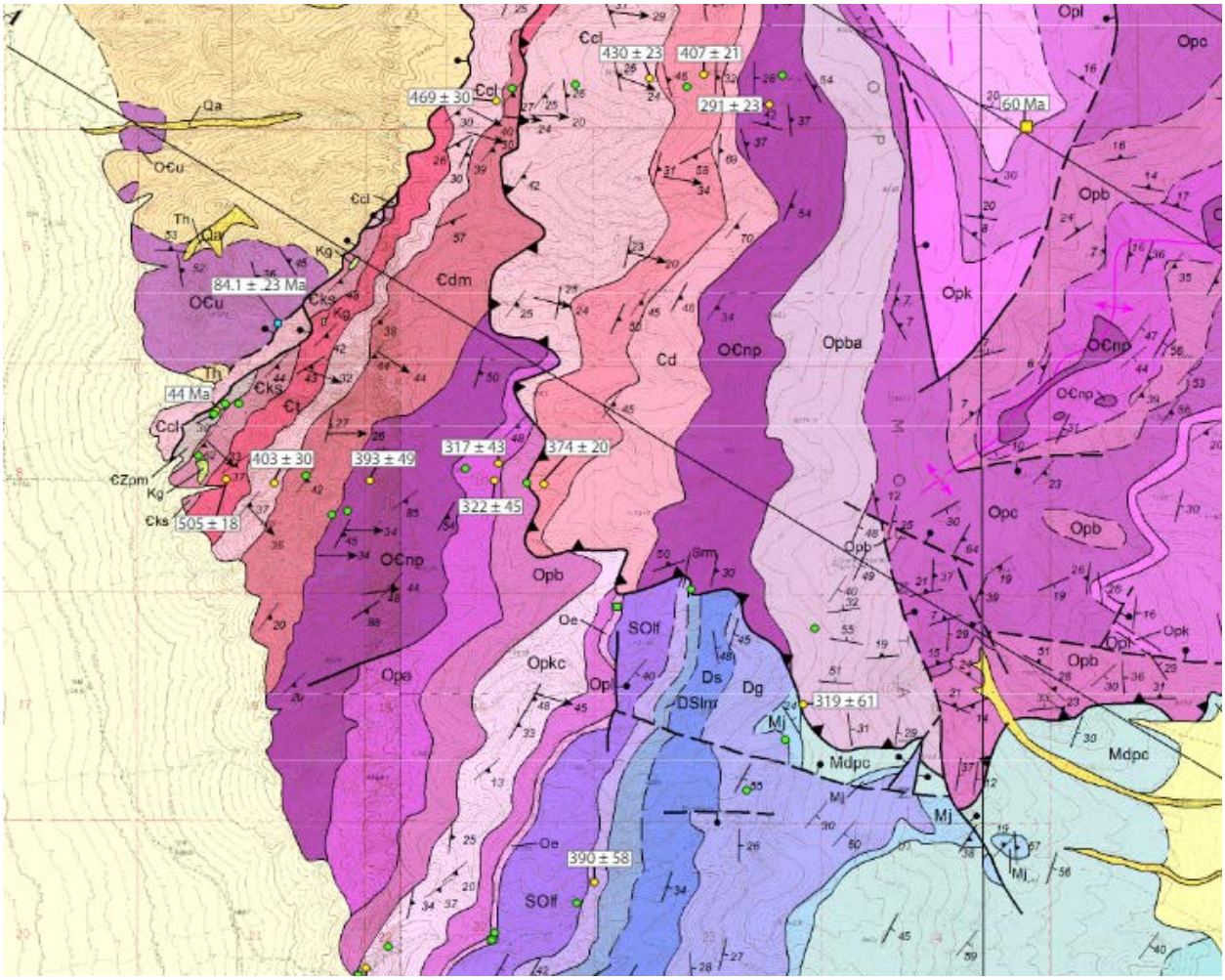

Figure 13. Temperature estimates for the Pequop Mountains from Howland (Keck 2016).

The Wood Hills are located centrally within the study area and contain same stratigraphic units to the Pequop Mountains, although at higher metamorphic grades and attenuated by as much as 50 percent (Camilleri, 1994; Camilleri and Chamberlin, 1997) (Figure.14). The timing of peak metamorphism due to Mesozoic contraction is inferred to be ~84 Ma based on U-Pb data from titanite (Camilleri and Chamberain, 1997; Camilleri, 2010). Metamorphic grade and grain size increases from lower amphibolite facies in the southeast to upper amphibolite facies in the northwest. In the northwest of the range, mylonites are exposed in the Wood Hills that show top-to-the-west to –northwest directed sense of shear (Camilleri, 2010). The mylonitic fabric is

most abundant in the extreme northwest corner of the range (Camilleri, 2010). Camilleri (2010) observed prophyroclast microstructures and CPO c-axes fabrics indicating noncoaxial flow consistently yielding such sense of shear. Quartz c-axis fabric opening-angle thermometry shows that the Wood Hills reached metamorphic temperatures of 380-515 °C (Jordan, Keck 2016). Plummer's (Keck 2016) crystallographic preferred orientation analysis indicates that samples within the Wood Hills were deformed by basal <a> slip, consistent with slip at these temperatures. Further, progressive changes in quartz grain size and the style of quartz recrystallization (subgrain to grain boundary migration from the south to the north) are consistent with increasing temperatures to the NW (Jordan, Keck 2016). Moving west from the mylonitic zone in the northwest portion of the Wood Hills described here, higher grade rocks in place are all from below the mylonitic shear zone, such as in Clover Hill.

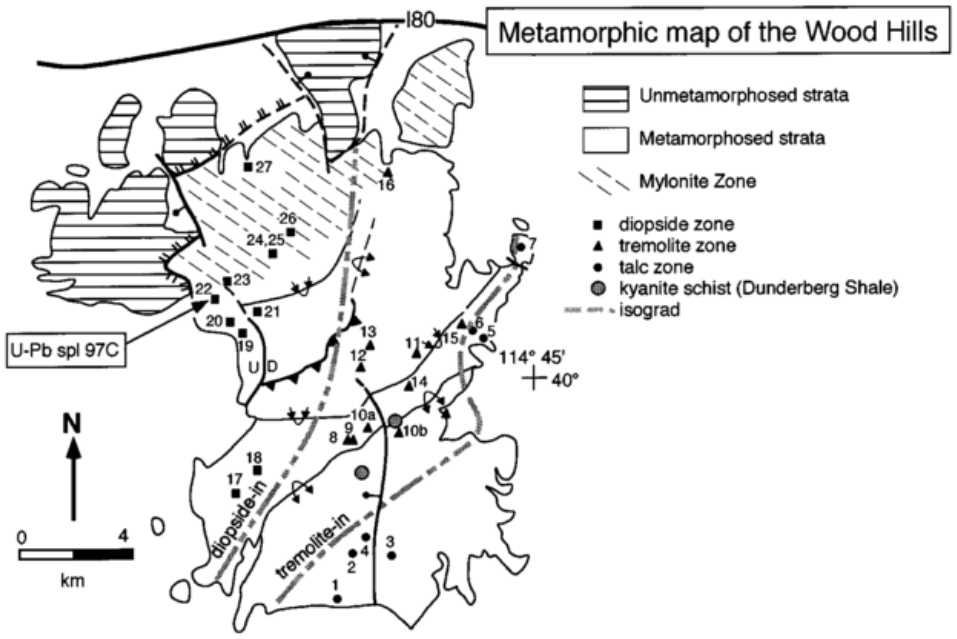

Figure 14. Metamorphic map of the Wood Hills. (from Camilleri and Chamberlin 1997)

Clover Hill is located in the western-most position and exposes the deepest structural levels and highest grades of metamorphism of the study area. A brittle, low-angle, normal-sense fault separates its hanging wall from its footwall (Sicard et al., 2011). The footwall consists of mylonitic Cambrian and Neoproterozoic metasedimentary strata. Structurally deeper, orthogniess and paragneiss make up the core of Clover Hill (Sicard et al., 2011). Thermobarometric constraints reported by Sicard et al. (2011) suggest conditions of ~0.8 GPa and 720-760 ˚C, signifying significant crustal thickening and high-temperature mylonitization.

Metamorphic Core Complex

Metamorphic core complexes form in regions with thick, gravitationally unstable crust and synextensional magmatism. In such regions, low-angle detachment faults, with brittle over-prints deform already ductily deformed rock (Armstrong, 1982) and rapidly exhume middle-crustal metamorphic rocks in the fault's footwall. The detachment fault cuts through the brittle and ductile deformation levels and with increasing depths from cataclastic rocks into regions where mylonites are dominant (Taugs, 2000) (Figure 15). The transition from brittle to ductile deformation generally occurs at lowest greenschist facies conditions. In the brittle crust of the upper block, faults or shear zones are associated with brecciation, cataclasis, and seismic slip (Taugs, 2000). The exposed succession in the footwall generally begins with deformation by non-coaxial laminar flow and amphibolite (800 °C / 0.8 GPa) or high greenschist facies conditions (500 °C / 0.6 GPa) (Taugs, 2000).

As the upper block slides off the lower block along the mylonitic detachment, the lower block is able to isostatically rebound towards the surface due to decompression and erosion. The upper block is intensely fractured and has been subjected to significant horizontal extension, with

multiple generations of high-angle normal faults that sole into the mylonitic detachment (Lister and Davis, 1989). The basic structure of a metamorphic core complex consists of a metamorphic basement core and an unmetamorphosed cover that are separated by a mylonitic detachment. In the brittle regime just above the mylonitic zone, a chlorite breccia often forms. The mylonitic influence lessens with depth below the mylonitic zone, grading into a partially mylonitic zone followed by a non-mylonitic crystalline core (Taugs, 2000). The exhumation of the lower plate is accompanied by a retrograde, uncomplete metamorphism, such as brecciation and fluid circulation during uplift (Taugs, 2000). The core of the complex is generally a gneiss dome, where the middle and lower crust has been dragged beneath the extensional detachment (Taugs, 2000). These structures are dome-like and form the highest topography in the region (Coney, 1980). In the North American Basin and Range Province, these structures are observed in a linear fashion from southern Canada to northern Mexico, where such tectonic activity was thought to have occurred (Coney, 1980).

Three models have been proposed to explain the exhumation of metamorphic core complexes. In the simple shear model, the low angle detachments accommodate extension, and in the rotated normal fault model, high angle normal faults rotate towards shallow dips progressively over time. Lastly, in the titled block model, straight faults bound rotating crustal blocks (Brun et al., 1994). Despite which model is used to describe a given area, multiple generations of detachment faults throughout the evolution of the core complex are thought to splay from one dominant fault. Faults observed at the surface are the youngest ones in a succession of the faults that have progressively unloaded the cover above the footwall, continuously exhuming and exposing footwall rocks to shallower crustal depths (Lister and Davis, 1989).

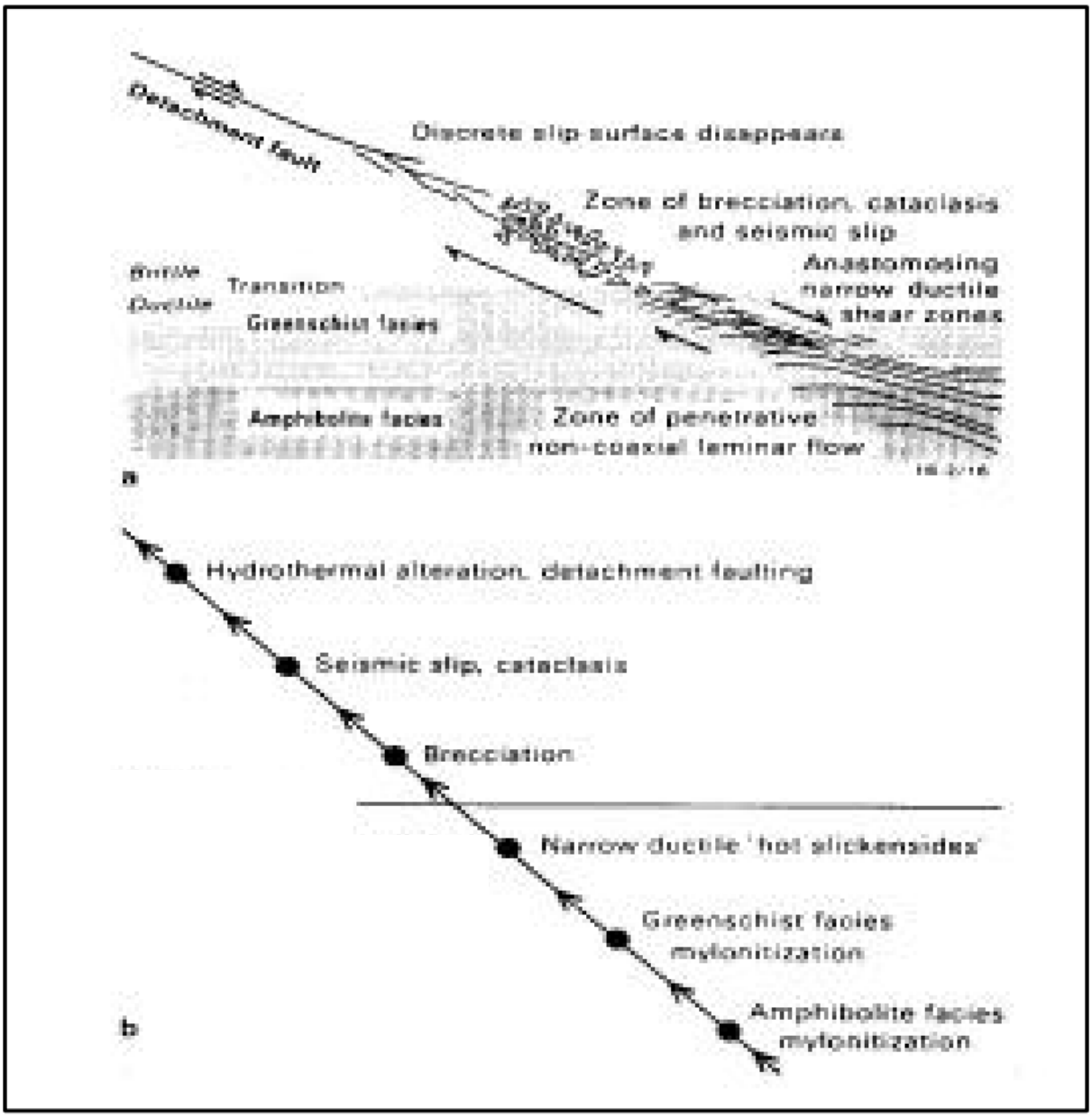

Figure 15. Shear zone diagram from Taugs (2000).

(U-Th)/He Thermochronology

It is well understood that temperature increases as a function of depth. Therefore, to understand the history or a rock's path from great depths and higher temperatures to shallow depths and cooler temperatures, we must understand how the rock cooled. Thermochronometry has emerged as a prominent tool for gaining insight into the tectonic history of metamorphic core complex rocks because it provides an estimate for the time elapsed since a sample passed through the respective closure temperature of the thermochronometric system being analyzed (Stockli, 2005). The effective closure temperature is the isotherm at which the mineral has cooled sufficiently to prevent diffusion of daughter product through radioactive decay of a parent (Reiners, 2005).

Thermochronology can provide insight into the timing, rate, and style of the tectonic and exhumational history of the rocks within the footwall of a detachment fault. Multiple chronometers with unique closure temperatures can be compared to create multi-stage, time-temperature histories in detail for a sample, if a geothermal gradient is assumed. For example, common thermochronometers include: $^{40}Ar/^{39}Ar$ hornblende (T_c = 500-550 $^{\circ}$C), mica (T_c = 300-370 $^{\circ}$C), and K-feldspar (T_c = 150-350 $^{\circ}$C); apatite fission-track (closure temperature 60 $^{\circ}$C, partial annealing zone 60-110 $^{\circ}$C, and totally annealed zone >110 $^{\circ}$C); zircon fission-track (closure temperature 240-250 $^{\circ}$C, partial annealing zone 230-310 $^{\circ}$C, and totally annealed zone >310 $^{\circ}$C); and lastly, (U-Th)/He (helium diffusivity temperature range varies widely by mineral assessed from 25-85 $^{\circ}$C for apatite to up to 240 $^{\circ}$C for zircon) (Stockli, 2005; Reiners, 2005; Ehlers et al., 2005) (Figure 16).

Zircon is highly suitable for thermochronology because it contains high U and Th concentrations, has high abundance in a wide range of lithologies, is refractory under

metamorphic and some magmatic conditions, and resists physical and chemical weathering (Reiners, 2005). The (U-Th)/He thermochronometer measures the accumulation of ^{4}He in a sample over time, due to the radioactive decay of uranium, thorium, and/or samarium. When a zircon is above the system's closure temperature (~180-200 °C), He diffuses out of the system and is not be retained in the sample; however, once the zircon cools past this closure temperature, He is retained (Figure 17). Effectively, the (U-Th)/He thermochronometer measures the time elapsed since the zircon cooled (or in the case of metamorphic core complexes: exhumed) past the closure temperature isotherm. This cooling could be associated with exhumation during normal faulting; in this case, rocks will cool (and therefore young) in the direction of slip. The potential is there to measure both the timing and rate of cooling (Stockli, 2005).

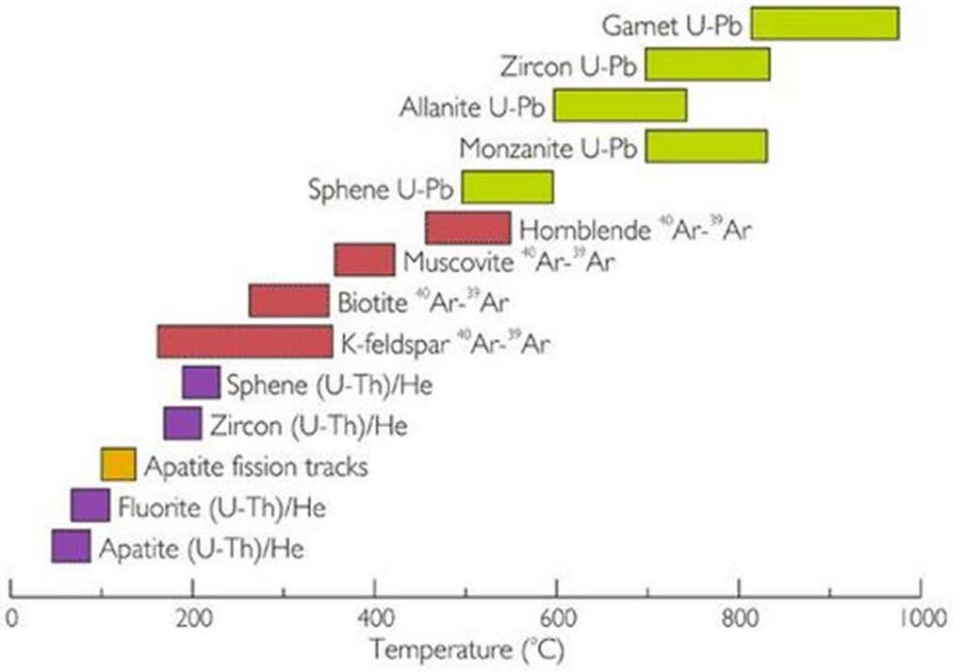

Figure 16. Closure temperatures for specific thermochronometers. (from John De Laeter Centre For Isotope Research at Curtin University)

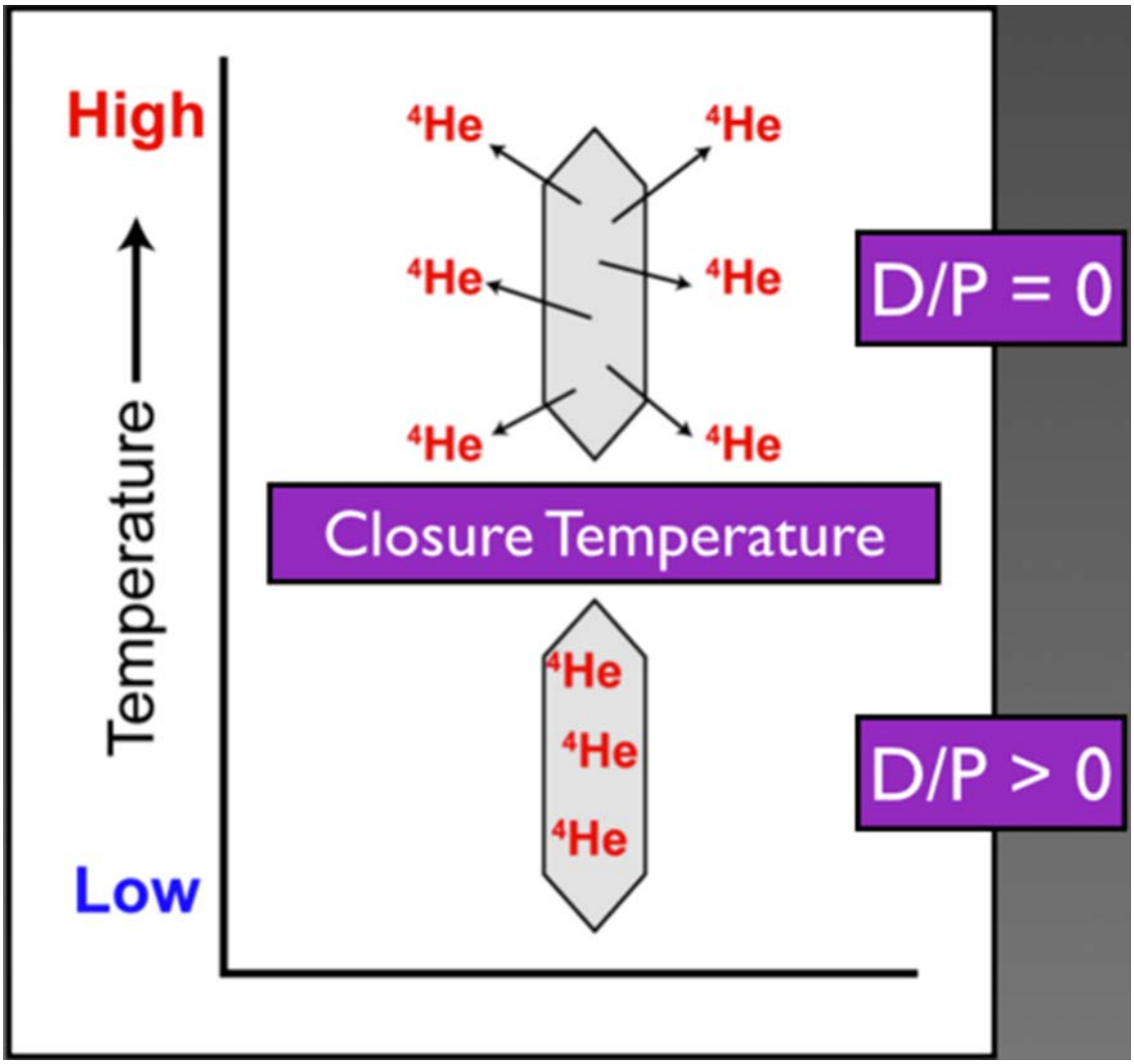

Figure 17. Simplified version of the zircon (U-Th)/He thermochronometric system. At temperatures greater than the closure temperature, helium produced during the radioactive decay of uranium, thorium, and samarium is diffused from the crystal. The daughter to parent ratio is zero. At temperatures lesser than the closure temperature, helium is retained within the crystal. The daughter to parent ratio is greater than zero. (from Apparentdip.wordpress)

METHODS

Field Work

Gallon-sized bags were filled with samples collected in the field from each location (Figure 18). Most samples (25) were collected from the Eureka Quartzite, an ideal target because it outcrops extensively across the entire study area and contains abundant zircon. Eureka Quartzite is Ordovician aged, fine-grained, white sandstone with sparse grey, graphite streaks that is sandwiched between the two, darker limestone and dolostone units of the Pogonip Group and the Ely Springs Dolomite (Camilleri, 2010). One sample was collected from the Prospect Mountain Quartzite (PMQ) in the footwall of the Independence Thrust in the Pequop Mountains. The Independence Thrust is a Mesozoic top-southeast thrust fault that cuts through the footwall of the Pequop Fault. In the Pequop Mountains, the PMQ is Precambrian-Cambrian aged, dark-grey quartzite with minor garnet-bearing micaceous layers (Camilleri, 2010). In the Pequop Mountains, one sample was collected from the footwall and one from the hanging wall of the Independence Thrust. One sample was collected on Clover Hill, from a flaggy, micaceous-feldspathic quartzite equivalent to the PMQ (Siccard et al., 2011). In the Wood Hills, samples were collected along a SE-NW transect in the direction of the supposed extension (Figure 18). One sample in the Wood Hills was collected from the thin sandstone formation at the base of the Simonson Dolomite Formation in the Wood Hills. Simonson sandstone is a red-brown-weathering, cross-bedded dolomitic sandstone. This sample was not used during the study because it did not contain viable zircons for analysis.

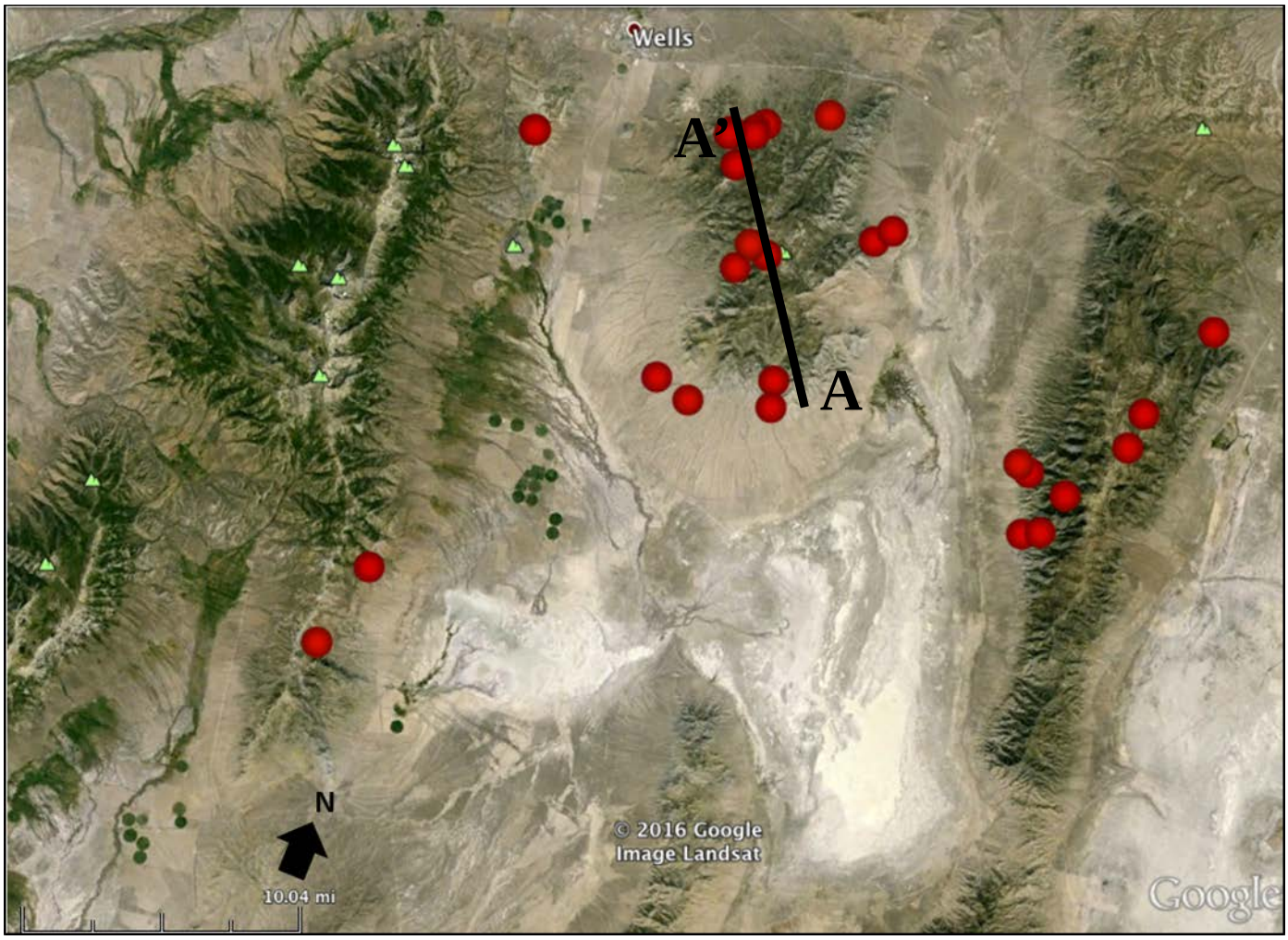

Figure 18. Spatial extent of sample collection. Transect of Wood Hills samples from southeast to northwest is shown in A-A'.

Mineral Separation

Standard mineral separation procedures were used to isolate zircon for dating. First, a half-gallon of each sample was crushed and pulverized at the University of Dayton using a jaw crusher and Bico Rock Pulverizer (see Figure 19 for all separation images). Next, at Washington and Lee University, samples were sieved in a rho-tap machine for 10 minutes to collect grains within the size range of 63-125 μm. A RP-4 Shaker Concentration Table was then used for density separation. The table's angle was altered at the start of each run to achieve aggressive separation (90-95% light and 5% heavy). Samples were sonicated in deionized water for 15 minutes to dissolve salt from the grains and subjected to multiple passovers by a bar magnet to prevent the machine jamming. Samples were passed through the Frantz Magnetic Separator three times at different magnetic amperage intensities (0.5, 1.0, and 1.5 amp) with the separator at a horizontal tilt of 5° and a vertical tilt of 20°. Lastly, non-magnetically separated samples were subjected to heavy liquids separation using sodium polytungstate.

Figure 19. Images of equipment used during separation

Zircon Grain Selection and (U-Th)/He Analysis

At Dr. Rebecca Flowers' Tectonics and Thermochronometry Lab, University of Colorado-Boulder, zircon grains were screened for quality (crystal size, shape, and presence of inclusions) and hand-selected using a binocular microscope in preparation for (U-Th)/He analysis (See Appendix A for Methods Explanation by Dr. James Metcalf) (see Figure 20 for images of grain selection process). Emphasis was placed on finding the largest grains with the most symmetric crystal shape; however, spherical or very well rounded grains were the best available specimens in some samples. Generally, three grains were collected and analyzed for each sample.

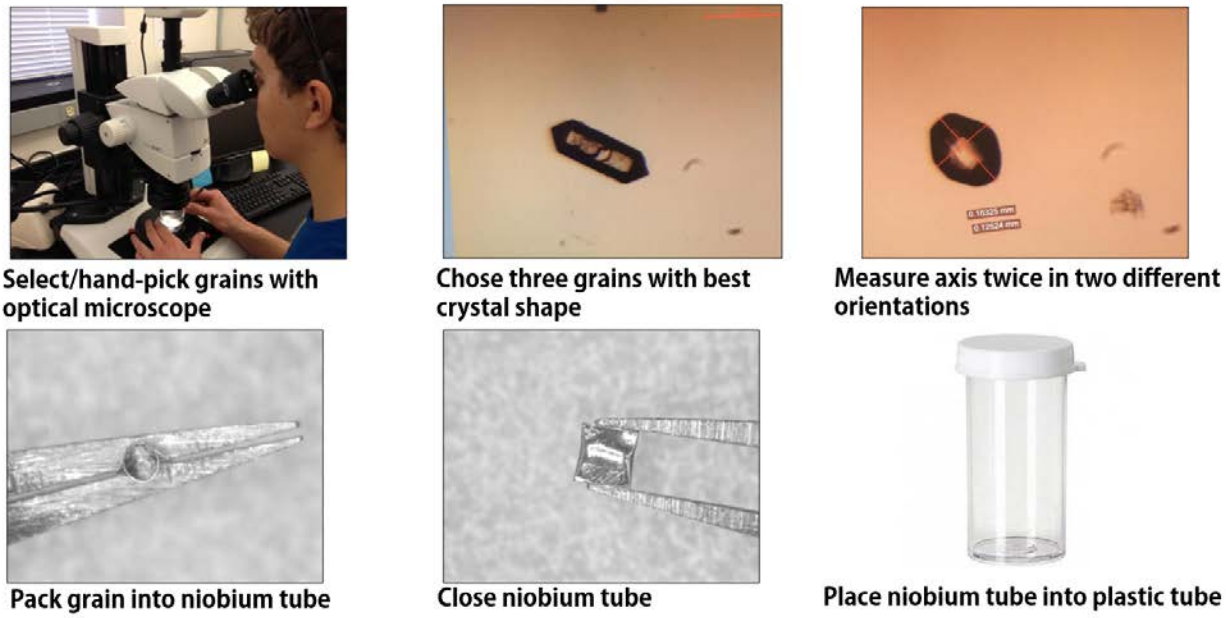

Figure 20. Images of steps required for grain selection.

The detailed methods for (U-Th)/He analysis below were provided by Dr. James Metcalf of the University of Colorado Boulder (see Appendix B for full text). Grains were placed into niobium tubes, loaded into an ASI Alphachron helium (He) extraction and measurement line,

heated to ~800-1100 °C with a diode laser for 5 to 10 minutes to extract the radiogenic ^{4}He, and then analyzed using a mass spectrometer (see Figure 19 for images of zircon (U-Th)/He analysis). Degassed grains were dissolved using Parr large-capacity dissolution vessels in a multi-step, acid-vapor dissolution process. First, samples were mixed with 200 µl of Optima grade HF and baked at 220 °C for 72 hours. Next, samples were mixed with 200 µl of Optima grade HCl and baked at 200 °C for 24 hours. Lastly, 200 µl of a 7:1 HNO_3:HF mixture was added to each sample and samples were cooked on a hot plate at 90 °C for 4 hours. Sample solutions, along with standards and blanks, were analyzed for U and Th. He dates were calculated using a custom spreadsheet provided by the Tectonics and Thermochronometry Lab.

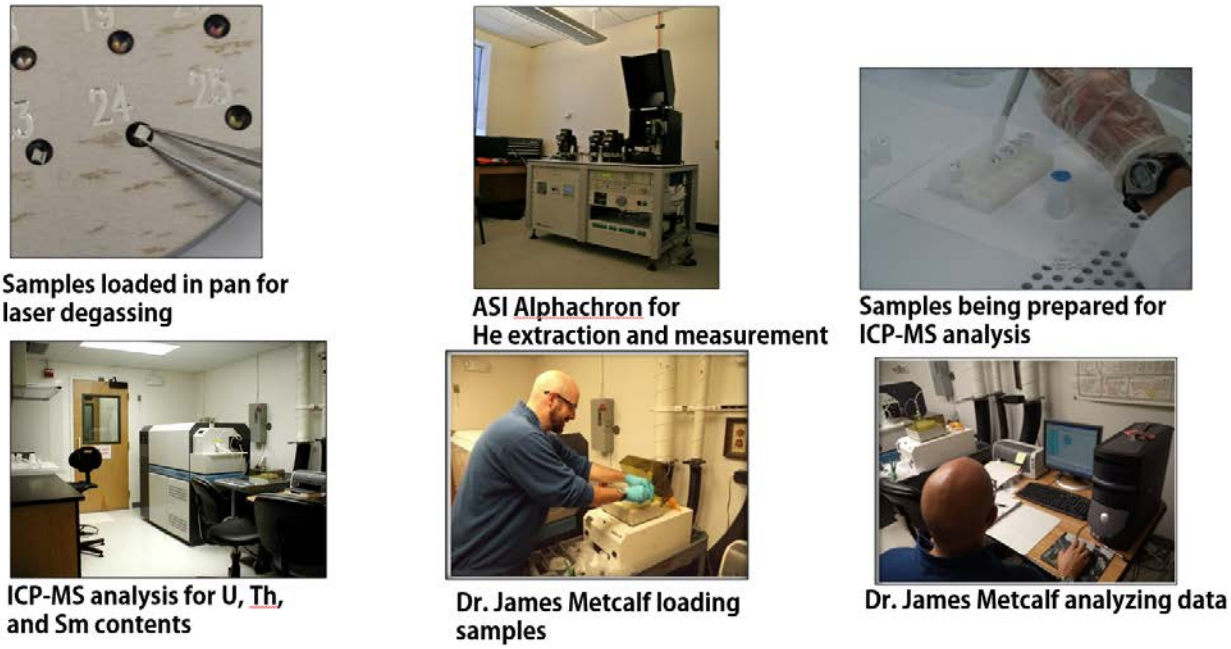

Figure 21. Images of steps required for zircon (U-Th)/He analysis.

RESULTS

Table 1a (abbreviated) reports the calculated apparent samples' ages from the zircon (U-Th)/He thermochronometry analyses along with the sample name, rock formation name, sample easting and northing, and elevation. Results are organized by the location of sample collection (Pequop Mountains vs. Wood Hills) (see Appendix A for full Table 1). The calculated uranium, thorium, and samarium contents are reported. The content of these elements has been shown to skew (U-Th)/He results (Reiners, 2005). High concentrations of uranium can lead to greater "effective uranium" (eU), which is a measurement of the total amount of radiation damage experienced by the crystal. Radiation damage can lead to increased release of helium gas over time as the crystal cools, resulting in greater helium retention and an older observed age; however, large amounts of radiation damage can limit the release of helium, resulting in a younger observed age (Guenthner et al., 2013; Reiners, 2005). Lastly, the radius (rs) of each sample is listed, which is the radius of a sphere with an equivalent surface area to volume ratio as the crystal undergoing analysis. The radius of the crystal is important because smaller crystals have larger surface to volume ratios and helium nuclei are required to travel shorter distances to free themselves from the crystal. In larger crystals, fewer helium nuclei are located near the edges of the crystal, comparatively, and therefore, less helium is lost during radiation (Reiners, 2005).

Cooling ages are Cenozoic and range from 60 Ma (in the Pequops) to as young as 24 Ma (in the Wood Hills) (Figure 22 & Figure 23) (See Appendix B for Table Element Explanation). Overall, all grains for a sample produced similar ages; exceptions are samples JR_D and JR_J. For these samples, there is a relationship between age and eU – this is because radiation damage

effects closure temperature (Guenthner et al., 2013). For JR_J, I will also use the average of three grains (36.77 Ma), which produced a spread of ages: 31.21 ± 2.26 Ma, 35.36 ± 2.57 Ma, and 43.76 ± 3.17 Ma.

Full Sample Name	Formation Name	Easting	Northing	Elevation	eU	Corrected Date (Ma)	Full Unc. (Ma)
Pequop Mountain Samples							
JR_3_z02	Eureka Quartzite	704226	4536310	9031	183.9	59.81	4.23
JR_3_z03	Eureka Quartzite	704226	4536310	9031	139.3	61.57	4.44
JR_A_z01	Prospect Mtn. Quartzite	698550	4534014	6156	357.9	44.36	3.23
JR_A_z03	Prospect Mtn. Quartzite	698550	4534014	6156	421.9	42.76	3.09
Wood Hills Samples							
JR_D_z01	Eureka Quartzite	677743	4548507	6568	470.8	22.88	1.65
JR_D_z02	Eureka Quartzite	677743	4548507	6568	73.7	40.43	3.21
JR_D_z03	Eureka Quartzite	677743	4548507	6568	79.8	43.21	3.16
JR_J_z01	Eureka Quartzite	680427	4542585	7450	79.2	43.76	3.17
JR_J_z02	Eureka Quartzite	680427	4542585	7450	193.8	31.21	2.26
JR_J_z03	Eureka Quartzite	680427	4542585	7450	74.4	35.36	2.57
JR_K_z01	Eureka Quartzite	681505	4542175	8102	179.7	34.68	2.48
JR_K_z02	Eureka Quartzite	681505	4542175	8102	65.9	35.73	2.66
JR_K_z03	Eureka Quartzite	681505	4542175	8102	237.4	32.59	2.31
JR_O_z01	Eureka Quartzite	678554	4546830	7416	107.3	28.49	2.04
JR_O_z02	Eureka Quartzite	678554	4546830	7416	107.3	27.76	2.01
JR_O_z03	Eureka Quartzite	678554	4546830	7416	170.5	24.78	1.77
JR_S_z01	Eureka Quartzite	683618	4535311	6343	47.3	40.38	2.97
JR_S_z02	Eureka Quartzite	683618	4535311	6343	94.7	40.46	2.90
JR_S_z03	Eureka Quartzite	683618	4535311	6343	91.0	36.87	2.67
JR_S_z04	Eureka Quartzite	683618	4535311	6343	92.8	36.96	2.67
Fish Canyon Tuff zircons run in conjunction with these samples yield a date of 30.2 ± 1.4 Ma (2s, n=3)							

Table 1a. Data from all samples analyzed in the study 'eU' is the effective Uranium, a measurement of the total amount of radiation experienced by the crystal, equivalent to U + .235Th. Corrected Date (Ma) is the alpha-ejection corrected age. 'Unc.' Is uncertainty. 'Ma' is million years since present.

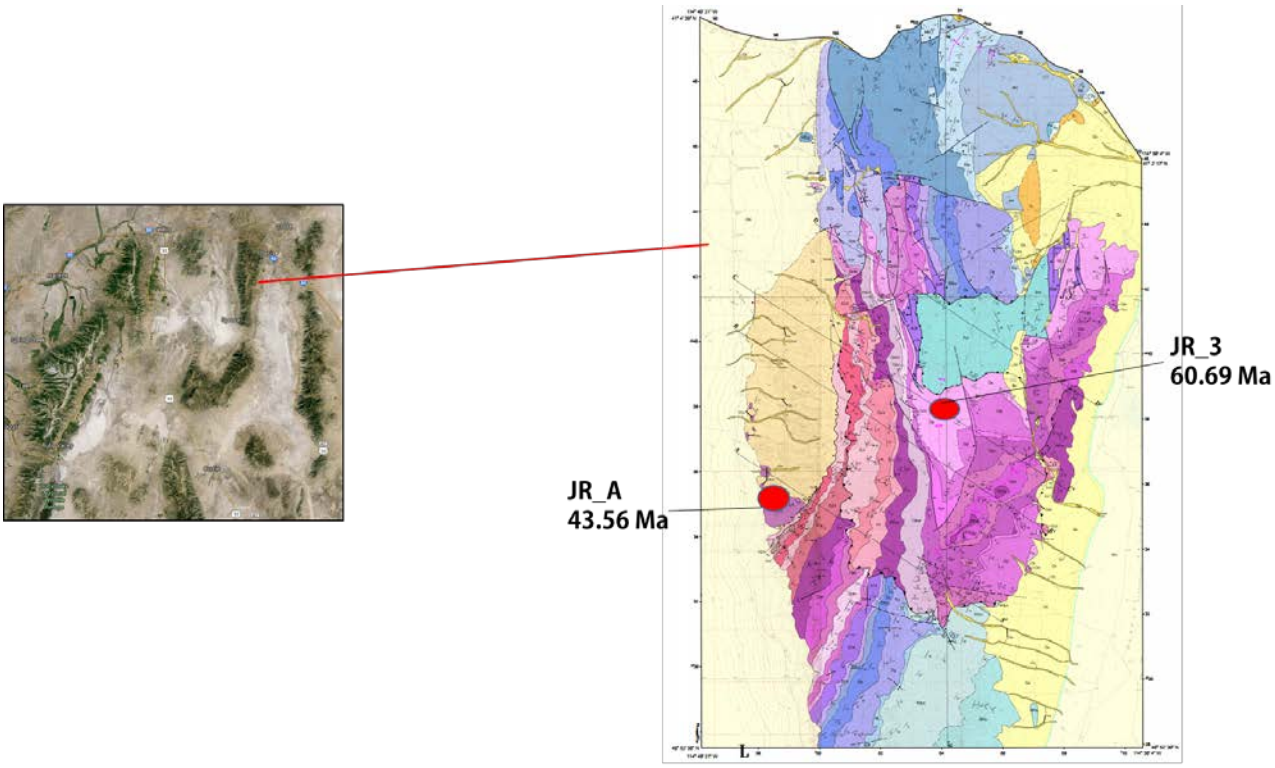

Figure 22. Pequop Mountains apparent age results.

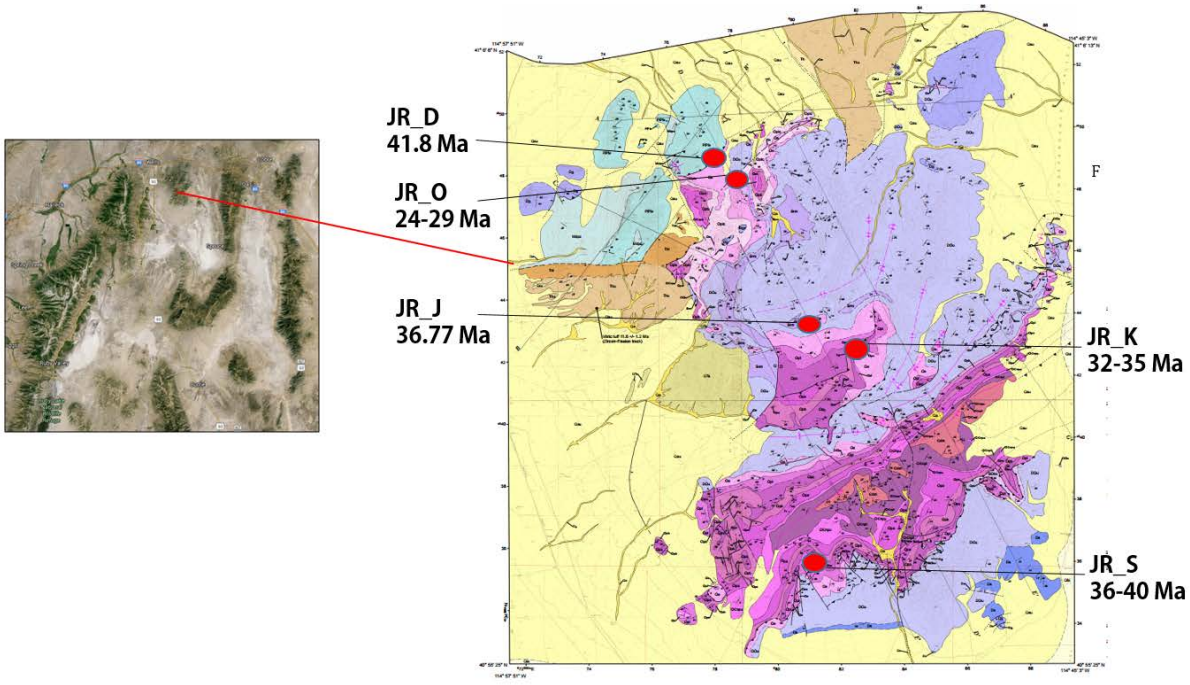

Figure 23. Wood Hills apparent age results.

For JR_D, two grains produced nearly identical ages (~41.8 Ma) and one grain produced an age of 21.18 ± 1.53 Ma. Interestingly, the grain with the dissimilar age has uranium content and eU values that are 7 times the value for the other two grains and likely a much lower closure temperature. The other two grains have eU values similar to others in the dataset. Therefore, I will use an average of the other two grains for subsequent data analysis and interpretation for JR_D. Notably, this sample was taken from within the hanging wall of a fault (Camilleri, 2010).

The two oldest samples are located within the Pequop Mountains (JR_A and JR_3). Grains for JR_3 indicate an age of ~60 Ma. JR_3 is located east of JR_A, whose grains produced ages ~43 Ma. The oldest ages in the Wood Hills are from the southernmost (JR_S) and northernmost (JR_D) samples. Excepting sample JR_D, the Wood Hills cooling ages young from the SE to the NW.

The sample from Clover Hill (JR_5) produced a diverse range of ages (71.02 Ma, 36.94 Ma, 21.18 Ma) (Figure 24). eU values are similar for each grain, but samarium values are tremendously high for grain one, whereas, the other two grains have zero concentration of samarium. Some factor seems to be effecting the apparent ages for this sample. Attention will not be given to this sample because the wide age range and lack of supporting samples prohibits further analysis.

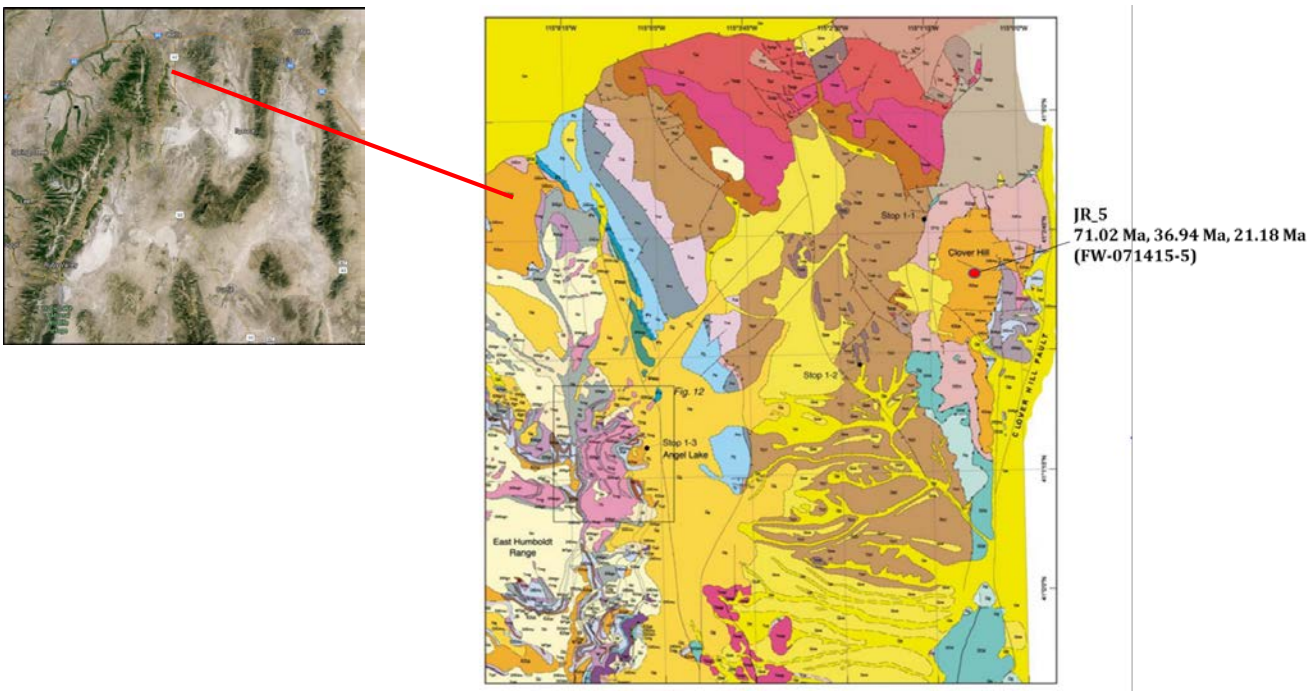

Figure 24. Clover Hill apparent age result.

DISCUSSION

Timing of the On-set of Exhumation on the Ruby Mountain Detachment Fault

The Wood Hills transect provides opportunity to document the time of cooling of footwall rocks exhumed along the Ruby Mountain Detachment fault. The method for determining the timing of the on-set of exhumation used in this study is the depth/distance method, as described by Stockli (2005). This method evaluates the apparent age pattern as a function of structural paleodepth (Figure 25). Sample transects are used to define inflection points in the age versus paleodepth arrays, which define the bounds of the partial retention zones. This method requires an estimation of the fault geometry and kinematics, which I assume to be southeast to northwest slip along the fault, consistent to what has been documented for the Ruby Mountains-East Humboldt Range. A sound understanding of the fault geometry and kinematics are needed because other processes such as fault dip changes with depth, secondary breakaway faults, and slip along multiple detachments can affect slip and exhumation rates.

Samples were at paleodepths greater than the partial retention zone prior to exhumation along the Ruby Mountain Detachment Fault (Camilleri, 2010) because metamorphism reached amphibolite grade (lower in SE to upper in NW) throughout the range due to peak conditions during Mesozoic contraction ~84 Ma (Camilleri, 2010). Therefore, we expected to not observe inflection points within our data, rather ages below the inflection point that trend systematically younger in the down-dip direction, recording progressive structural unroofing (Stockli, 2005). Additionally, it is assumed that samples were collected along a near-horizontal structural transect parallel to the extensional fault slip direction, as is proposed by Stockli (2005).

Samples within the transect young towards the northwest, which indicate that they were exhumed along this fault (Figure 26). As mentioned above (see Geologic Setting), the 150 km mylonitic shear zone in the NW that bounds the Ruby Mountains and East Humboldt Range along strike is well described with kinematic indicators consistent with top-NW shear (MacCready et al., 1997; Plummer & Jordan, Keck 2016). The sense of shear is also well-described in the northwestern portion of the Wood Hills, where it displays the same sense of direction (Camilleri, 2010).

In the northwestern Wood Hills, where samples O and D were collected, rocks generally show mylonitic overprinting (Jordan, this volume) (Figure 27). Quartz fabrics in some samples show top-NW shearing and top-NW CPO. Dislocation creep processes associated with mylonitization and grain-size reduction that form such CPOs require deformation temperatures of at least 350-400 °C (frictional to viscous transition for the Tonale fault zone in the Italian Alps at 280 ± 30 °C) (Stipp et al., 2004). Therefore, samples were deformed at temps well-above those of zircon He closure and cooling ages must post-date deformation. Sample JR_O from this study records a zircon (U-Th)/He age of 24-29 Ma. Jordan (Keck 2016) performed CPO analysis on this same sample, demonstrating mylonitization in the shear zone. Mylonitzation must predate 24-29 Ma, and therefore, slip must have been active prior to this sample's exhumation through the ~180-220 °C isotherm. In addition, Eocene age samples throughout the rest of the Wood Hills suggest that the on-set of extension could be Eocene or older. This finding is in contrast to the findings by Colgan et al. (2010), who document a later onset of extension in the Ruby Mountains to the south.

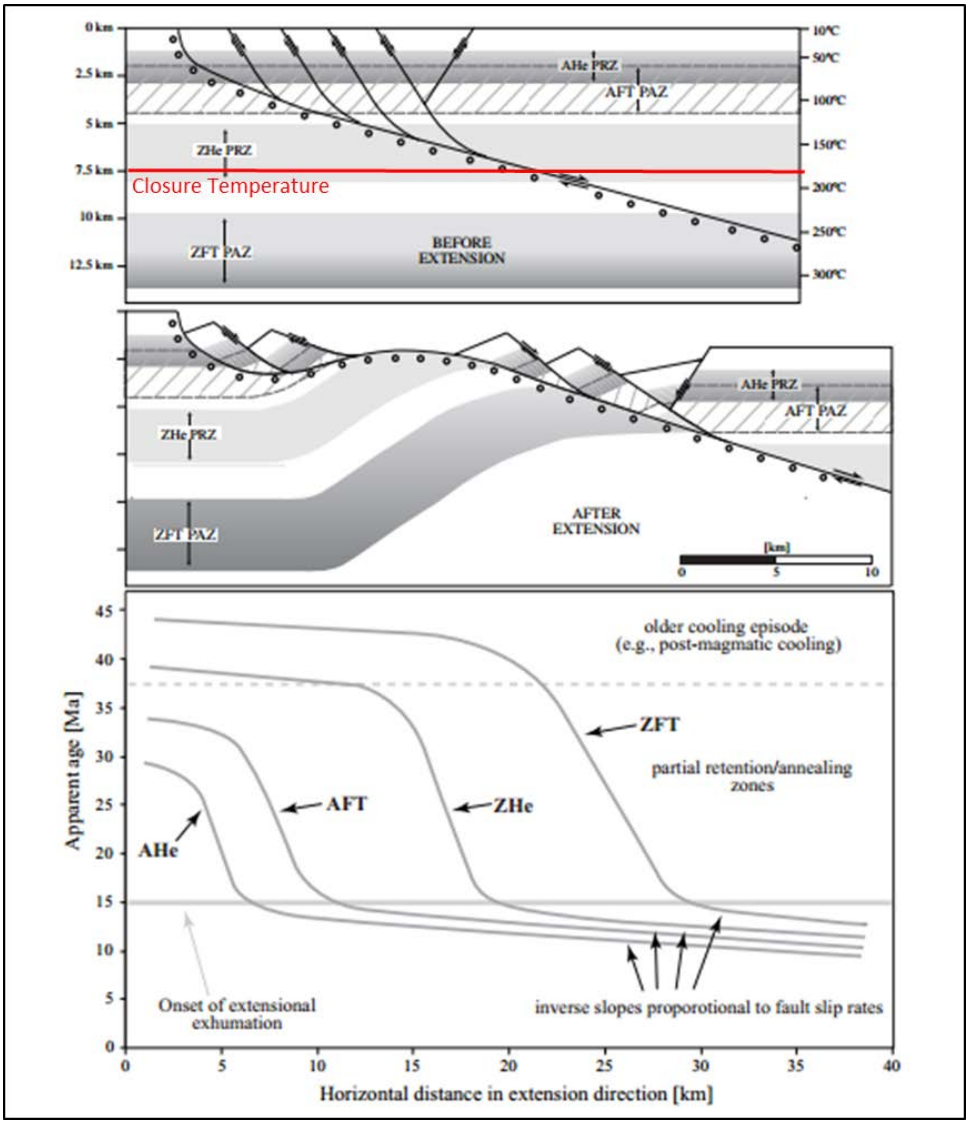

Figure 25. Illustration of the structural evolution and exhumation of footwall rocks. Circles represent samples collected in the direction of tectonic transport. Lower diagram depicts schematic age-distance relationships for different thermochronometers in such a scenario. Above the partial retention zone, ages trend younger in the direction of transport. This inverse of this slope can be used to estimate fault slip rates. (from Stockli, 2005).

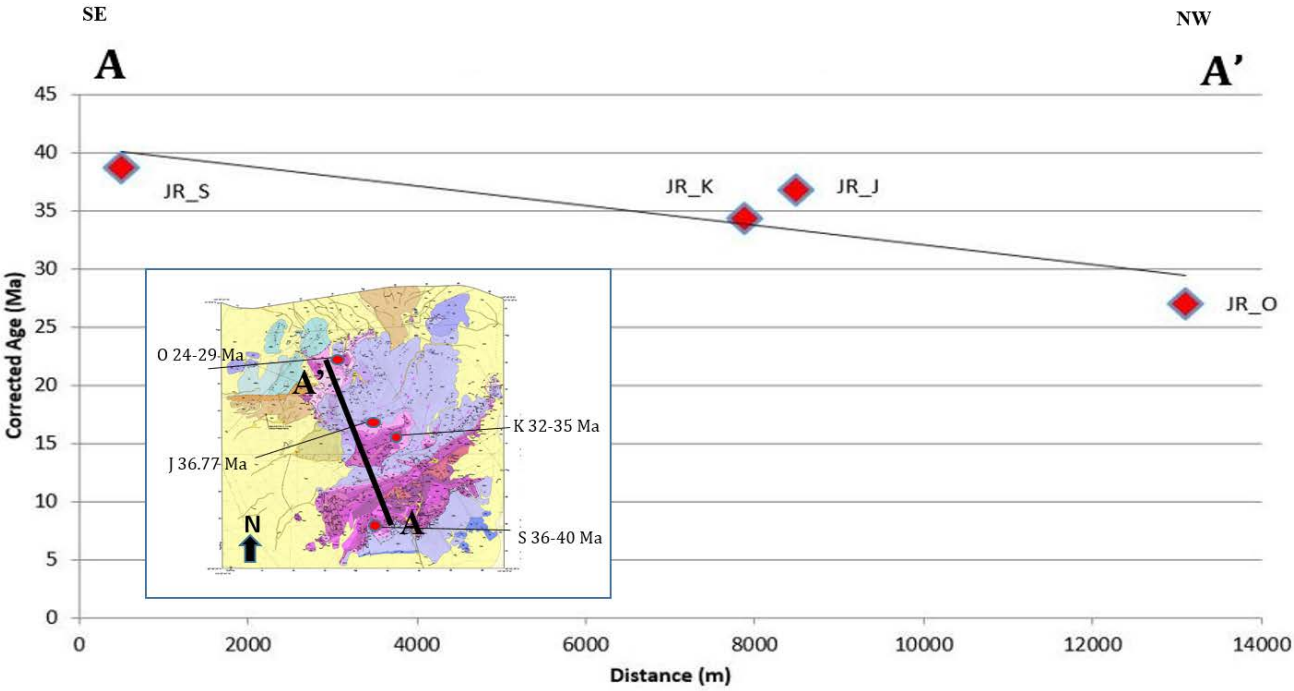

Figure 26. Plot of cooling age vs. distance along the transect in the direction of tectonic transport. Samples young towards the northwest in the direction of slip along the Ruby Mountain Detachment Fault.

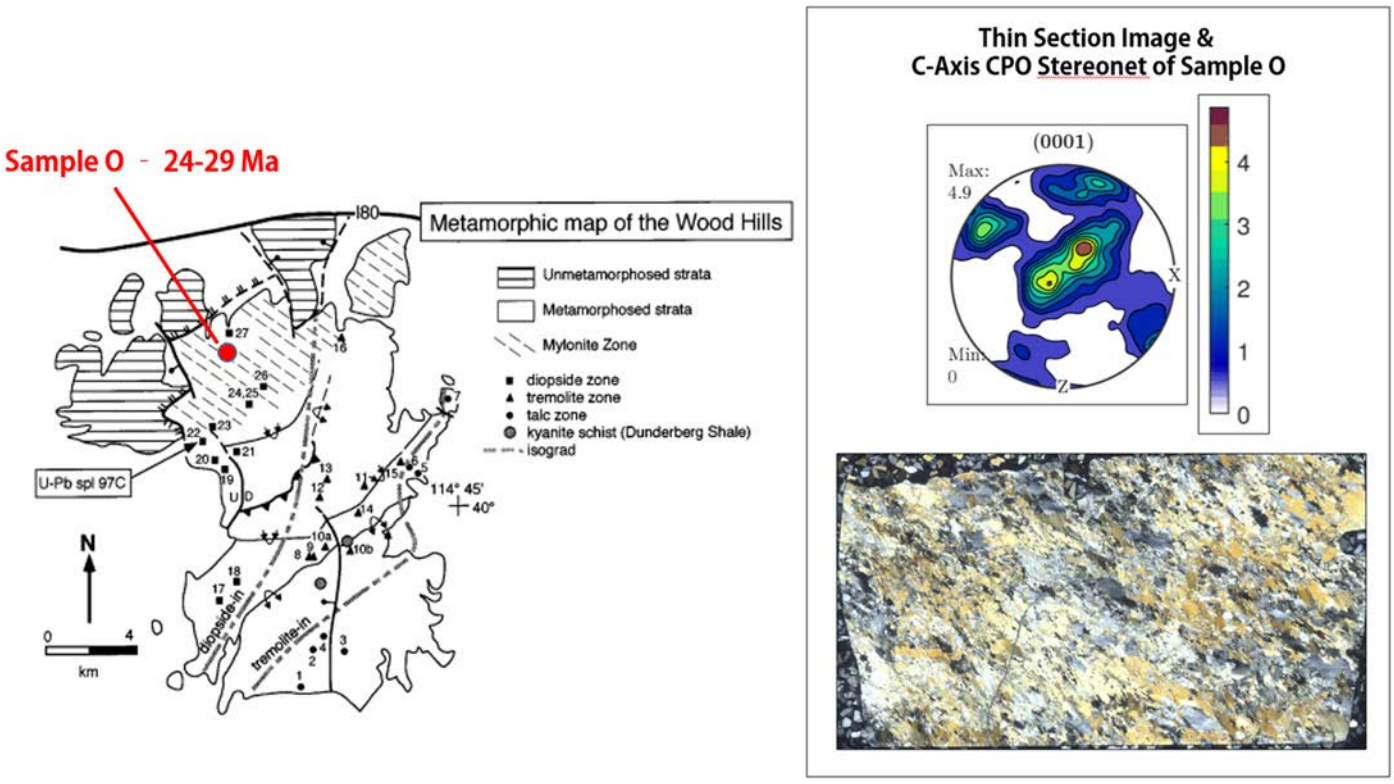

Figure 27. Sample JR_O in the northwest region of the Wood Hills exhibits a strong mylonitic fabric, consistent with slip along the Ruby Mountain Detachment Fault. CPO data from Jordan (Keck, 2016).

The information provided in this study and by Gifford et al. (2008) provides sufficient evidence to extend the chrontours proposed by McGrew and Snee (1994) eastward across the Wood Hills (Figure 30). In Figure 28, biotite $^{40}Ar/^{39}Ar$ ages, which record passage through a closure temperature ~300 °C, were used to generate chrontours (lines of equal age) for the exhumation of the East Humboldt Range in McGrew and Snee's (2008) study. Ages calculated from our study with the zircon (U-Th)/He system are used to create new chrontours with geometries similar to the chrontours proposed by McGrew and Snee (1994). A similar geometry is appropriate for these chrontours because the kinematics of the mylonitic zone in the northwest of the Wood Hills matches that for the mylonitic zone along the western margin of the East

Humboldt Range, which provides sufficient evidence to conclude that both areas were exhumed in a similar style (MacCready et al., 2007; Plummer & Jordan, Keck 2016; Camilleri, 2010). Additionally, the two samples collected near each other in the central Wood Hills in this study (JR_K & JR_J ~35 Ma) along the length of a proposed chrontour, exhibit similar ages, which provides further evidence for chrontours of such geometry.

Two muscovite $^{40}Ar/^{39}Ar$ ages by Gifford et al. (2008), which record passage through a closure temperature of ~300 °C, are used to construct an additional new chrontour across the central Wood Hills. The geometry of this chrontour matches those for the rest of the Wood Hills, assuming the kinematics of exhumation were not altered drastically as the Wood Hills samples cooled from ~400-200 °C.

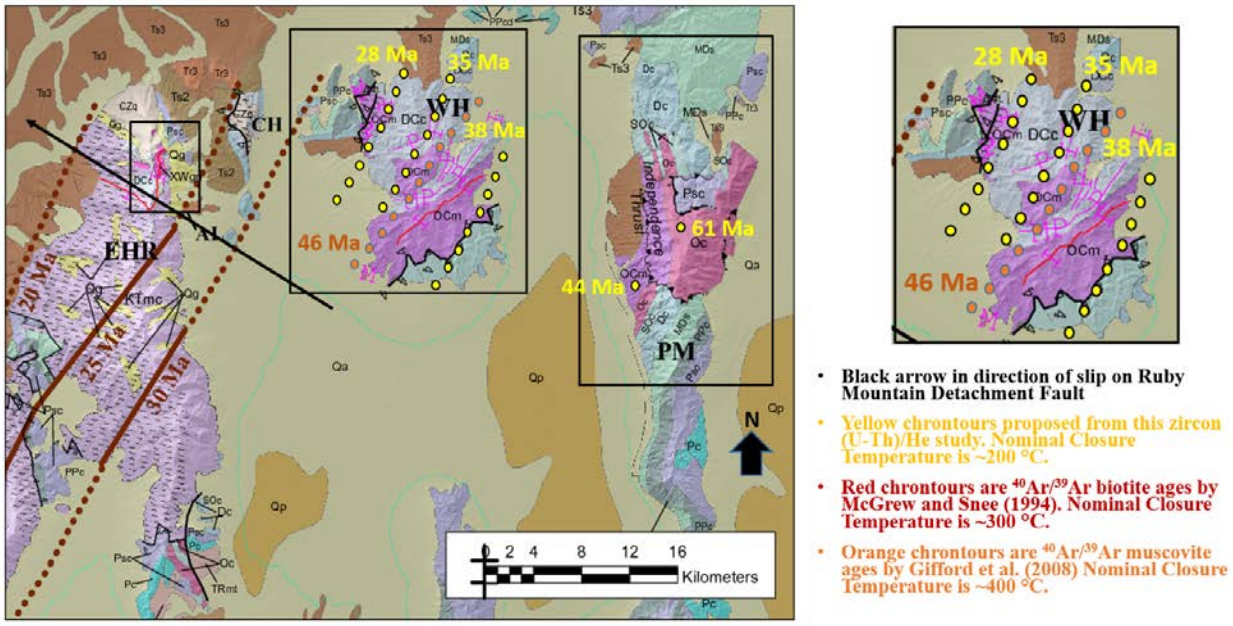

Figure 30. Proposed chrontours for the Wood Hills as a result of this study.

The Rate of Exhumation on the Ruby Mountain Detachment Fault

My zircon helium ages can be compared with two muscovite $^{40}Ar/^{39}Ar$ ages from the Wood Hills to provide estimates for the rate of slip along the Ruby Mountain Detachment Fault and the rate of cooling of the rocks during exhumation (Gifford et al., 2008) (Figure 28). Muscovite $^{40}Ar/^{39}Ar$ records the time since a sample has passed through the 400 °C isotherm. Sample DF02-221 is from a quartz vein and the muscovite gave an age of 43.7 ± 5.3 Ma (89% ^{39}Ar, MSWD = 4.50). H03WH-42 is a marble and produced an age of 49.3 ± 3.6 Ma (75% ^{39}Ar, MSWD = 5.40). Samples JR_J (31-44 Ma) and JR_K (32-35 Ma) are located closest to the Wood Hills samples, DF02-221 (43.7 ± 5.3 Ma) and H03WH-42 (49.3 ± 3.6 Ma), reported by Gifford et al. (2008). Taking the average of the two zircon (U-Th)/He samples (~35 Ma) and of the two muscovite $^{40}Ar/^{39}Ar$ samples (~46 Ma), these results indicate that rocks within this portion of the Wood Hills rapidly cooled ~200 °C over 10 Ma (20 °C/Ma). This is slower than the consistently rapid cooling rates (>40-100 °C) reported for the complexes further south in Colorado River extensional corridor (Foster and John, 1999). However, during the lifetime of a detachment fault, cooling rates are expected to be variable (Ruppel et al., 1988).

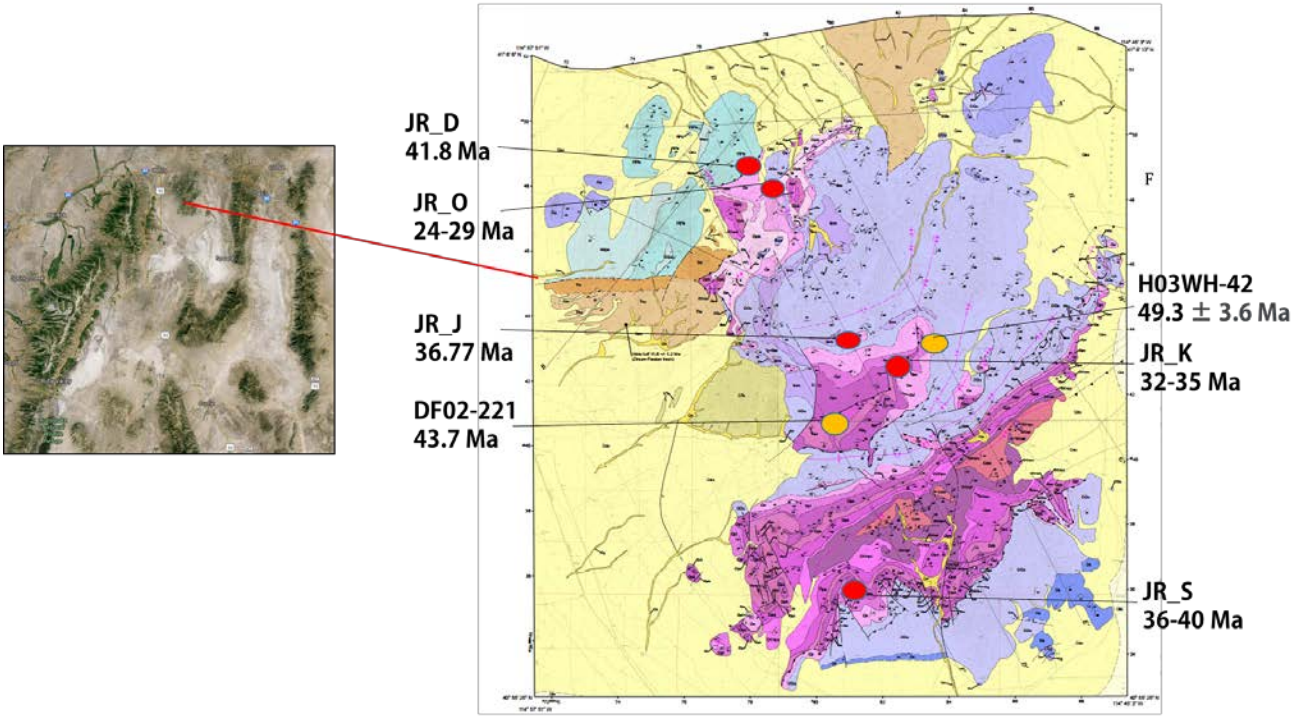

Figure 28. Incorporating age results from Gifford et al. (2008) for the Wood Hills. Samples from this study are represented by red circles. Samples from Gifford et al. (2008) are represented by yellow circles.

It can be assumed that ages will progressively young in the direction of tectonic transport on a detachment fault as samples progressively exhume from greater depths within the footwall upwards through the zircon (U-Th)/He closure temperature with continued slip along a detachment fault (Stockli, 2005; Foster and John, 1999). Samples at higher structural levels will pass through first, which will produce older apparent ages, followed by the passage of increasingly lower structural levels, which will produce younger apparent ages. Rates of slip on detachment faults may be estimated by examining the inverse slope of the apparent age with distance in the slip direction for samples that were deeper than the partial retention zone (thermochronological system with zero age) prior to extension (Foster and John, 1999). Low-temperature thermochronometers are best suited for this purpose because it is possible that high-

temperature thermochronometers yield complex cooling ages and the effects of thermal pulses on apparent age is a problem at lower crustal levels (Foster and John, 1999). Additionally, isotherms must remain approximately horizontal during exhumation, which is thought to occur during a few million years after the onset of exhumation (Ketcham, 1996).

In the Wood Hills, the apparent age data indicate that cooling and exhumation occurred progressively from the southeast towards the northwest, which is evidence that the Wood Hills were exhumed along the Ruby Mountain Detachment Fault. It appears that there was at least ~13 km of extension (distance from JR_S to JR_O) over ~13 Ma, which indicates a slip rate of ~1 km/Ma. Although it has been documented by Burbank (2002) that progressive erosion is capable of exhuming terranes at much faster rates than estimated here, the trend from southeast to northwest is inconsistent with erosional exhumation (Snee et al., 2016). Additionally, no thick sediment packages from the Eocene or Oligocene consistent with this hypothesis have been documented as evidence of such a history.

The rate estimate is consistent with estimates of slip rates on the modern Wasatch Fault (< 1km/Ma), which bounds the western margin of the Wasatch Mountains, just east of Salt Lake City and ~400 km east of this study site (Mattson and Bruhn, 2001). This is a slower slip rate than observed for other metamorphic core complexes; for example, Brichau et al. (2006) estimated a slip rate of ~6-8 km/Ma for the core complex in Naxos, Greece. The Central Menderes metamorphic core complex in western Turkey is suspected to have a slip rate ~2 km/Ma (Gessner et al., 2001). Mylonites in the Woodlark spreading ridge of the D'Entrecasteaux Islands, Papa New Guinea, have been exhumed along a detachment due to >50 km of slip at rates >12 km/Ma (Little et al., 2007).

Additionally, Foster and John (1996) estimated much faster slip rates for the Colorado Extensional Corridor, a classic example of detachment faulting and metamorphic core complex development in the Southern Basin and Range province, which is about 900 km south of the Wood Hills. For the Buckskin core complex, they estimated a rate of 7.7 ± 3.6 km/Ma. For the Harcuvar Mountains core complex, they estimated a rate of 6.5 ± 3.0 km/Ma. For the Whipple Mountains, they estimated a slip rate of 7.8 ± 4.4 km/Ma. For the North Plomosa Mountains and Chemeheuvi Mountains, they estimated much slower slip rates (3.0 ± 1.0 km/Ma & 3.3 ± 0.9 km/Ma), yet still three times the estimate for the Wood Hills. Both temperature and distance over time analyses indicate that exhumation of the Wood Hills was relatively slow when compared with other metamorphic core complexes of the Basin and Range Province and globally.

Farther north, in the Okanogan dome of central Washington, zircon (U-Th)/He thermochronology indicates a slip rate of 3.7 km/Ma on the detachment fault from 51 to 41 Ma (Toraman, 2014). In the northern Rocky Mountains of southwestern Montana, slip on the detachment fault of the Anaconda metamorphic core complex between ~50-39 Ma was on the order of 1 km/Ma (Foster et al., 2010). Grice (2006) produced similar estimates for the Anaconda metamorphic core complex using muscovite and biotite $^{40}Ar/^{39}Ar$ thermochronology.

Reconnaissance Analysis of the Pequop Mountains

The Pequop Mountains are composed of the highest structural levels within the study area, and it is possible that they were exhumed with the Wood Hills and Ruby Mountains-East Humboldt Range on the Ruby Mountain Detachment Fault. Two reconnaissance samples from the Pequop Mountains were analyzed to determine if they are part of the larger core complex system. These samples provide new context on the cooling history of the upper levels of the core complex.

New metamorphic temperature estimates (Howland, Keck 2016) indicate that the Pequop Mountains samples (JR_A & JR_3) reached temperatures at which they should have been reset following burial (Figure 29). He found that the rocks closest to sample JR_A in the footwall of the Independence Thrust in the Pequop Mountains recorded peak temperatures of 400-520 °C. His study does not include peak temperatures less than 2 km away from sample JR_3; however, he reported temperatures decreasing away from the hanging wall towards the east. The two temperatures closest to the hanging wall were 291 ± 23 °C and 407 ± 21 °C. Therefore, it is reasonable to assume sample JR_3 reached peak temperatures lower than JR_A, perhaps, in the range of 200-400 °C.

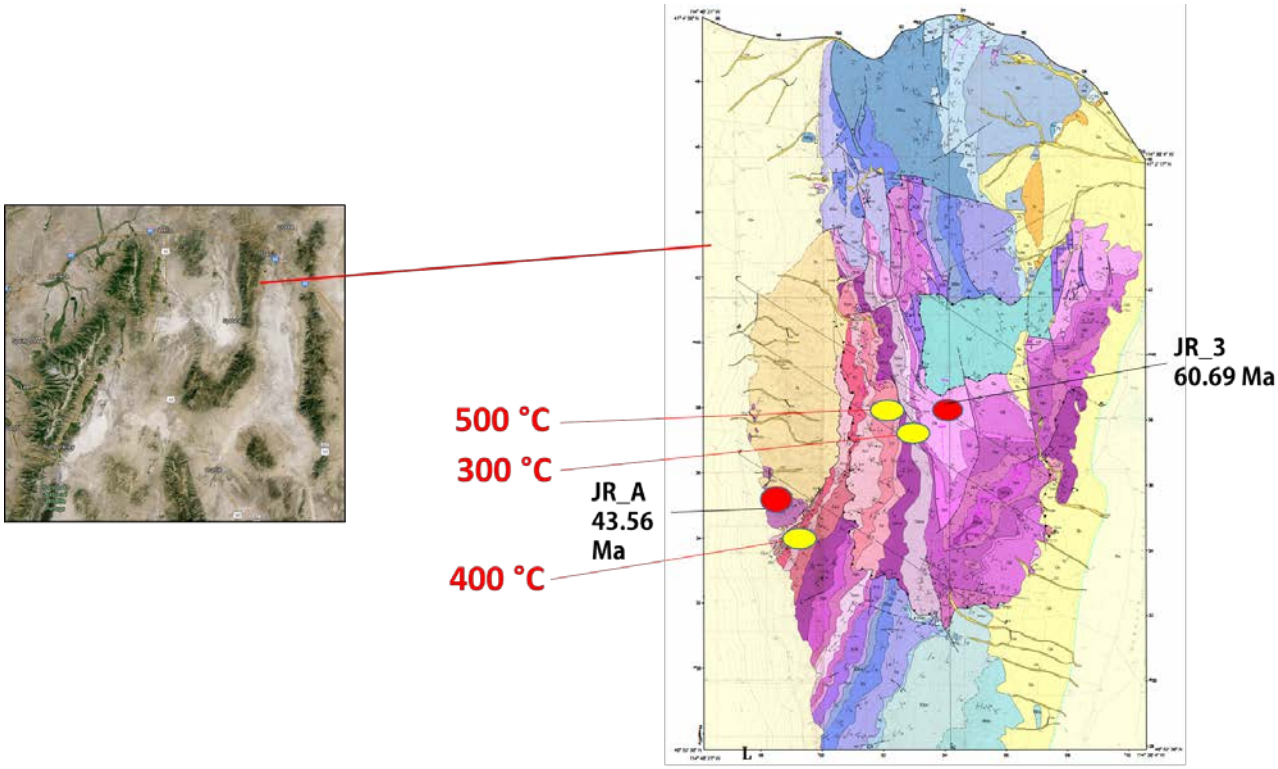

Figure 29. Incorporating Howland (Keck 2016) temperature estimates with apparent ages determined by this study.

Due to the zircon (U-Th)/He age of ~60 Ma calculated in this study for JR_3 (Ordovician depositional age Eureka Quartzite sample), it is clear this rock reached temperatures deeper than the closure temperature for zircons (180-220 °C) following deposition and that samples were reset. The same can be said about JR_A (Cambrian aged Prospect Mountain Quartzite sample), which yielded an apparent age of ~43.56 Ma. As expected, the sample from the higher structural level produced an older apparent age.

The subsequent exhumation could be due to several possibilities, including (1) slow cooling due to progressive erosional exhumation, and (2) cooling due to extension, which suggests that slip along the Ruby Mountain Detachment Fault began as early as 60 Ma. Although only two samples were analyzed for this study, they preserve the trend of younging

towards the west that is observed in the Wood Hills and Ruby Mountains-East Humboldt Range. This is probably not too surprising given that metamorphic grade increases towards the west. Additionally, JR_A demonstrates a cooling age that is older than JR_S, the sample further towards the southeast in the Wood Hills, which is consistent with it possibly being a part of the continual exhumation of the core complex along the detachment fault. If the zircon (U-Th)/He chrontours for the Wood Hills in Figure #, where extended further east towards the Pequop Mountains at similar ~1 Ma/Km distance intervals, then JR_A would be very close to the 44-47 Ma chrontours.

Further investigation is needed to draw conclusions because it is possible that these samples cooled slowly due to progressive erosional exhumation of the high plateau following extreme crustal thickening during the Mesozoic. According to Burbank (2002), rates of unloading greater than a few mm/a have generally been attributed to tectonic exhumation through extensional processes and erosion by surface processes has been given a minor role. There is a widespread perception that erosional rates are unlikely to exceed 1 mm/a and that surface processes are incapable of producing rapid rates of unloading (Burbank, 2002). However, he argues that rates of up to ~10 mm/a due to erosion may dominate the unloading processes in high terranes. Additionally, although sediment loads carried by rivers can be used to estimate the impact of erosion on exhumation, no deposition has been documented such activity. Therefore, it is plausible that the exhumation of the Pequop Mountains was due to continued erosion, and there is inconclusive evidence to determine that they were part of the broader core complex exhumation due to slip on the Ruby Mountain Detachment Fault, since it is proven that erosion can have a significant impact on exhumation.

Sample JR_D

Sample JR_D is an interesting sample because it yielded two distinct dates: 22.88 ± 1.65 Ma and 40-43 ± 3 Ma (the second is an average of dates from two grains). This sample's results can be interpreted in several ways. First, if the ~23 Ma age is correct, this grain represents a continuation of the younging trend towards the northwest. For example, just south of this sample, JR_O gave an age of 24-29 Ma. However, if ~40-43 Ma is a more accurate age for this sample, it is not clear how to explain the deviation from the broader trend in ages across the Wood Hills and more sampling is needed. Interestingly, this sample was taken from within the hanging wall of a fault mapped by Camilleri (2010). It is possible that this sample was located structurally higher and passed through the zircon (U-Th)/He closure temperature isotherm earlier than the nearby samples for which we calculated ages. Then later and at shallower crustal level, this sample was dropped down to deeper structural levels by the fault mapped by Camilleri (2010) to its present position. A second explanation of this sample's location in the footwall of another fault (~1.5 km further NW than the fault just discussed) (Figure 14) is possible. It may be that this sample was located at a depth near the zircon (U-Th)/He closure temperature just before slipping on this smaller fault, which would have occurred prior to slipping on the more dominant fault. This would exhume JR_D past the closure temperature prior to motion by JR_O.

CONCLUSION

Key study results are: (1) the Ruby Mountain Detachment Fault was active before Eocene times (24-29 to 36-40 Ma) and exhumed the Wood Hills through the zircon (U-Th)/He closure temperature isotherm (~180-220 °C), (2) the SE-NW trend in exhumation of the Wood Hills matches the trend suggested for the Ruby Mountain Detachment Fault in the broader study area, (3) the Wood Hills were exhumed relatively slowly (cooling ~20 °C/Ma & slipping ~1 km/Ma), and (4) the footwall and portions of the hanging wall of the Independence Thrust within the Pequop Mountains reached temperatures great enough to reset zircon (U-Th)/He ages; however, more sampling is needed to confirm that the Pequop Mountains were exhumed along the Ruby Mountain Detachment Fault.

ACKNOWLEDGMENTS

I would like to thank the Keck Geology Consortium, the National Science Foundation, and ExxonMobil Corporation for allowing me to participate in this unique research opportunity. I want to express my gratitude to Dr. Rebecca Flowers and Dr. James Metcalf for allowing me to use their Thermochronology Lab. I am also thankful for the Washington and Lee Geology Department and the Marcellus H. Stow Award, which provided additional funds to travel and complete the lab work in Boulder. I am extremely gracious for the continual guidance from Dr. Allen McGrew (University of Dayton), and the help in the field from Dr. Zelalem Bedaso (University of Dayton) and Dr. Matthew Manon. Lastly, I am very thankful for such a wonderful advisor, who was always excited and willing to help me along the way. Dr. Rahl's enthusiasm was the heartbeat to this operation. Thank you.

WORKS CITED

Armstrong, R., 1982, Cordilleran metamorphic core complexes – from Arizona to southern Canada: Annual Review in Earth and Planetary Sciences, no. 10, p. 129-154.

Bogen, N., and Schweickert, R., 1985, Magnitude of crustal extension across the northern Basin and Range province: constraints from paleomagnetism: Earth and Planetary Science Letters, no. 75, p. 93-100.

Brichau, S., Ring, U., Ketcham, R., Carter, A., Stockli, D., and Brunel, M., 2006, Constraining the long-term evolution of the slip rate for a major extensional fault system in the central Aegean, Greece, using thermochronology: Earth and Planetary Sciences Letters, no. 241, p. 293-306.

Brun, J., Sokoustis, D., and Van Den Driessche, J., 1994, Analogue modeling of detachment fault systems and core complexes: Geology, no. 22, 319-322.

Burbank, D., 2002, Rates of erosion and their implications for exhumation: Mineralogical Magazine, Vol. 66(1), p. 25-52.

Camilleri, P., 1994, Mesozoic and Cenozoic tectonic and metamorphic evolution of the Wood Hills and Pequop Mountains, Elko County, Nevada [Ph.D. dissert.]: Laramie, Wyoming, University of Wyoming, 196 p.

Camilleri, P., 2010, Geologic map of the Northern Pequop Mountains, Elko County, Nevada: Nevada Bureau of Mines and Geology Map, no. 171.

Camilleri, P., 2010, Geologic map of the Wood Hills, Elko County, Nevada: Nevada Bureau of Mines and Geology Map, no. 172.

Camilleri, P. and Chamberlain, K., 1997, Mesozoic tectonics and metamorphism in the Pequop Mountains and Wood Hills region, northeast Nevada: Implications for the architecture and evolution of the Sevier orogeny: Geological Society of America Bulletin, v. 109, p. 74-94.

Camilleri, P., 1998, Prograde metamorphism, strain evolution, and collapse of footwalls of thick thrust sheets: a case study from the Sevier hinterland, U.S.A.: Journal of Structural Geology, v. 20, p. 1023-1042.

Colgan, J., Howard, K., Fleck, R., and Wooden, J., 2010, Rapid middle Miocene extension and unroofing of the southern Ruby Mountains, Nevada: Tectonics, Vol. 29.

Coney, P., 1980, Cordilleran metamorphic core complexes: GSA Memoir, no. 153, Geological Society of America, p. 7-34.

Curtin University. John De Laeter Centre For Isotope Research [Internet]. 2013. Curtin University. Curtin University. [cited 2013/10/28]. Available from: http://jdlc.curtin.edu.au/research/geochron.cfm.

Dallmeyer, R., Wright, J., Secor, D., and Snoke, A., 1986, Character of the Alleghanian orogeny in the southern Appalachians: Part 2. Geochronological constraints on the tectonothermal evolution of the eastern Piedmont in South Carolina: Geological Society of America Bulletin, v.97, no. 11, p. 1329-1344.

Decelles, P.G., 2004, Late Jurassic to Eocene evolution of the Cordilleran thrust belt and Foreland basin system, western U.S.A.: American Journal of Science, Vol. 304, p. 105-168.

Ehlers, T., 2005, Crustal thermal processes and the interpretation of thermochronometer data: Reviews in Mineralogy & Geochemistry, no. 58, p. 315-350.

Evans, S., Styron M., C. van Soest, M., Hodges, K., and Hanson, A., 2015, Zircon and apatite (U-Th)/He evidence for Paleogene and Neogene extension in the Southern Snake Range, Nevada, USA: Tectonics, no. 34.

Foster, D and Barbara, J., 1999, Quantifying tectonic exhumation in an extensional orogeny with thermochronology: examples from the southern Basin and Range Province: Exhumation Processes: Normal Faulting, Ductile Flow and Erosion. Geological Society, London, Special Publications, no. 154, p. 343-364.

Foster, D., Grice Jr., W., Kalakay, T., 2010, Extension of the Anaconda metamorphic core complex: $^{40}Ar/^{39}Ar$ thermochronology and implications for Eocene tectonics of the northern Rocky Mountains and the Boulder batholith: Lithosphere, Vol. 2, no. 4, p 232-246.

Garver, J, 2002, Fission-track laboratory procedures at Union College: Union College, v. 2.72.

Gessner, K., Ring, U., Johnson, C., Hetzel, R., Passchier, C., Gungor, T., 2001, An active bivergent rolling-hinge detachment system: Central Menderes metamorphic core complex in western Turkey: Geology, Vol. 29, no. 7, p. 611-614.

Gifford, J, 2008, Quantifying Eocene and Miocene extension in the Sevier hinterland in Northeastern Nevada: Masters Thesis to University of Florida.

Grice, W., 2006, Exhumation and cooling history of the middle Eocene Anaconda metamorphic core complex, western Montana: University of Florida Masters Thesis.

Guenthner W., Reiners, P., Ketcham, R., Nasdala L., and Giester, G., 2013, Helium diffusion in natural zircon: Radiation damage, anisotropy, and the interpretation of zircon (U-Th)/He thermochronology: American Journal of Science, no. 313, p. 145-198.

Henry, C., 2009, Uplift of the Sierra Nevada, California: Geology, Vol. 37, no. 6, p. 575-576.

Howard, K., 2003, Crustal structure in the Elko-Carlin region, Nevada, during Eocene gold mineralization: Ruby-East Humboldt metamorphic core complex as a guide to the deep crust: Economic Geology, v. 98, p. 249-268.

Ketchum, R., 1996, Thermal models of core complex evolution in Arizona and New Guinea: Imlpications for ancient cooling paths and present-day heat flow: Tectonics: no. 15, p. 933-951.

Kistler, R., Ghent, E., and O'Neil, J., 1981, Petrogenesis of garnet two-mica granites in the Ruby Mountains, Nevada: Journal of Geophysical Research, no. 86(B11), p. 10591-10606.

Lister, G. and Davis, G., 1989, The origin of metamorphic core complexes and detachment faults formed during Tertiary continental extension in the northern Colorado River region, U.S.A.: Journal of Structural Geology, Vol. 11, no. 1/2, p. 65-94.

Little, T., Baldwin, S., Fitzgerald, P., Monteleone, B., 2007, Continental rifting and metamorphic core complex formation ahead of the Woodlark spreading ridge, D'Entrecasteaux Islands, Papa New Guinea: Tectonics, Vol. 26, no. 1.

Long, S.P., Thompson, S.N., Reiners, P.W., and DiFiori, R.V., 2015, Synorogenic extensionlocalized by upper-crustal thickening: An example from the Late Cretaceous Nevadaplano, Geology, Vol. 43, p. 351-354.

MacCready, T., Snoke, A., Wright, J., and Howard, K., 1997, Mid-crustal flow during Tertiary extension in the Ruby Mountains core complex, Nevada

Mattson, A., Bruhn, R., 2001, Fault slip rates and initiation age based on diffusion equation modeling: Wasatch Fault Zone and eastern Great Basin: Journal of Geophysical Research, Vol. 106, no. B7, p. 13,739-13,750.

McGrew, A. and Casey, M., 1998, Quartzite fabric transition in a Cordilleran metamorphic core complex: Fault-related Rocks: A photographic atlast, p. 484-489.

McGrew, A. and Snee, L., 1994, $^{40}Ar/^{39}Ar$ thermochronologic constraints on the tectonothermal evolution of the northern East Humboldt Range metamorphic core complex, Nevada: Tectonophysics, no. 238, p. 425-450.

McGrew, A., Snoke, A., Geologic map of parts of the Welcome and Humboldt Peak 7.5' quadrangles, East Humboldt Range-Clover Hill area, Elko County, Nevada: unpublished data.

Miller, D., Repetski, J., and Harris, A., 1991, East-trending Paleozoic continental margin near Wendover, Utah: Society of Economic Paleontologists and Mineralogists, Pacific Section, no. 67, p. 439-461.

N.A., 2014, Thermochronology, Apparentdip.wordpress.com/2014/07/19/thermochronology

Reiners, P., 2005, Zircon (U-Th)/He thermochronometry: Reviews in Mineralogy & Geochemistry, Vol. 58, p. 151-179.

Reiners, P. and Brandon, M., 2006, Using thermochronology to understand orogenic erosion: Annual Review of Earth and Planetary Science, no. 34, p. 419-466.

Ruppel, C., Royden, L., and Hodges, K., 1988, Thermal modeling of extensional tectonics: Application to the pressure-temperature-time histories of metamorphic rocks: Tectonics, no. 7.

Sonder, L., and Jones, C., 1999, Western United States Extension: How the west was widened: Annual Review of Earth and Planetary Sciences, no. 27, p. 417-462.

Siccard, K., Snoke, A., and Swapp, S., 2011, The metamorphic and structural history of Clover Hill, Nevada, part of the Ruby-East Humboldt Core Complex: Rocky Mountain (63rd Annual) and Cordilleran (107th Annual) Joint Meeting, Vol. 43, No. 4, p. 15.

Snee, L.W., Miller, E.L., Grove, M., Hourigan, J.K. and Konstantinou, A., 2016, Cenozoic paleogeographic evolution of the Elko Basin and surrounding region, northeast Nevada: Geosphere, Vol. 12, no. 2.

Snell, K., Koch, P., Druschkle, P., and Eiler, J., 2014, High elevation of 'Nevadaplano' during the Late Cretaceous: Earth and Planetary Sciences Letters, no. 386, p. 52-63.

Sousa, J., 2008, Kinematic analysis of mylonitic rocks, Southern Ruby Mountains, SW Montana: Evidence for Proterozoic orogenic crustal thickening and topographic collapse: Undergraduate Review, no. 4, p. 57-63.

Spencer, J., Reynolds, S., 1991, Tectonics of mid-Tertiary extension along a transect through west central Arizona: Tectonics, no. 10, p. 1024-1221.

Stipp, M., Stünitz, R., Heilbronner, R., and Schmid, S., 2002, The eastern Tonale fault zone: a "natural laboratory" for crystal plastic deformation of quartz over a temperature range from 250 to 700 °C: Journal of Structural Geology, no. 24, p. 1861-1884.

Stockli, D., 2005, Application of low-temperature thermochronometry to extensional tectonic settings: Reviews in Mineralogy & Geochemistry, Vol. 58, p. 411-448.

Taugs, D., 2000, Metamorphic Core Complexes: Bergakademie Freiberg, Technishe Universitat.

Toraman, E., 2014, Late-stage exhumation of metamorphic core complexes and landscape development during orogenic collapse of the North American Cordillera: University of Minnesota Ph.D. Dissertation.

Wernicke B., and Snow J., 1998, Cenozoic tectonism in the central Basin and Range: Motion of the Sierran-Great Valley block: International Geology Review, no. 40, p. 403–410

Wright, J. and Snoke, A., 1993, Tertiary magmatism and mylonitization in the Ruby-East Humboldt metamorphic core complex, northeastern Nevada: U-Pb geochronology and Sr, Nd, Pb isotope geochemistry: Geological Society of America Bulletin, v. 105, p.935-952.

APPENDIX A – FULL DATA TABLE

Full Sample Name	length 1 (µm)	width 1 (µm)	length 2 (µm)	width 2 (µm)	2X Term	Dim Mass (µg)	rs (µm)	4He (nmol/g)	±	U (ppm)	±
JR_3_z02	279.7	95.0	278.1	97.9	Y	6.31	58.77	47.500	0.066	158.19	2.82
JR_3_z03	159.9	108.7	157.6	96.1	Y	4.04	57.20	36.794	0.031	121.29	2.30
JR_5_z01	231.4	96.8	234.2	98.0	Y	7.40	60.01	66.177	0.069	197.89	6.86
JR_5_z02	274.7	99.7	267.3	96.8	Y	9.23	62.52	47.766	0.040	281.03	4.86
JR_5_z03	329.0	107.2	325.5	107.8	Y	13.73	69.66	25.667	0.021	261.30	4.44
JR_A_z01	142.6	65.8	143.5	68.9	Y	2.07	40.18	62.283	0.076	348.50	6.57
JR_A_z03	170.2	77.1	170.6	82.0	Y	3.45	47.55	74.588	0.088	397.97	7.16
JR_D_z01	166.3	99.6	165.0	94.8	Y	4.43	53.56	45.975	0.042	461.55	9.00
JR_D_z02	143.1	99.6	135.5	75.5	Y	2.55	48.36	12.134	0.020	61.41	1.72
JR_D_z03	171.3	114.7	166.6	112.9	Y	5.60	58.58	15.011	0.026	70.23	1.66
JR_J_z01	301.6	107.8	307.3	101.8	Y	11.96	67.29	15.561	0.009	71.46	1.24
JR_J_z02	270.3	94.5	272.6	94.4	Y	8.65	60.58	26.555	0.051	183.36	3.31
JR_J_z03	254.9	90.0	257.7	96.3	Y	7.82	59.17	11.462	0.013	65.13	1.16
JR_K_z01	239.0	146.4	236.7	147.4	Y	14.04	79.12	28.799	0.024	167.07	3.01
JR_K_z02	160.0	107.2	158.3	103.9	Y	4.60	54.78	10.101	0.018	59.67	1.26
JR_K_z03	163.3	125.2	176.7	121.5	Y	6.20	60.63	34.034	0.033	232.31	4.00
JR_O_z01	204.6	148.3	203.1	137.2	Y	10.10	78.59	14.015	0.010	95.56	1.70
JR_O_z02	245.5	118.3	247.7	117.2	Y	8.32	69.36	13.332	0.013	95.86	2.04
JR_O_z03	186.6	101.3	187.3	101.0	Y	4.66	58.54	18.162	0.025	143.78	2.59
JR_S_z01	187.4	141.1	186.5	141.3	Y	9.07	76.48	8.734	0.010	42.87	0.87
JR_S_z02	176.4	149.1	168.6	153.1	Y	9.59	78.71	17.554	0.017	76.71	1.38
JR_S_z03	175.6	133.1	165.8	139.6	Y	7.72	72.81	15.192	0.018	83.08	1.59
JR_S_z04	157.7	140.7	157.4	145.6	Y	7.86	73.75	15.568	0.008	85.73	1.50

Full Sample Name	Th (ppm)	±	Sm (ppm)	±	eU	4He (ncc)	±	U (ng)	±	Th (ng)	±	Sm (ng)	±
JR_3_z02	109.44	4.33	0.14	2.38	183.9	6.721	0.009	0.9986	0.018	0.6909	0.027	0.0009	0.015
JR_3_z03	76.50	6.71	2.71	5.09	139.3	3.328	0.003	0.4895	0.009	0.3087	0.027	0.0109	0.021
JR_5_z01	56.23	4.45	87.95	7.02	211.1	10.975	0.011	1.4642	0.051	0.4161	0.033	0.6508	0.052
JR_5_z02	47.63	3.45	0.00	0.00	292.2	9.878	0.008	2.5930	0.045	0.4395	0.032	0.0000	0.000
JR_5_z03	29.71	2.14	0.00	0.00	268.3	7.899	0.006	3.5875	0.061	0.4079	0.029	0.0000	0.000
JR_A_z01	40.01	13.01	0.00	0.00	357.9	2.888	0.004	0.7210	0.014	0.0828	0.027	0.0000	0.000
JR_A_z03	101.83	7.87	4.14	9.22	421.9	5.764	0.007	1.3722	0.025	0.3511	0.027	0.0143	0.032
JR_D_z01	39.23	6.09	7.02	17.97	470.8	4.562	0.004	2.0435	0.040	0.1737	0.027	0.0311	0.080
JR_D_z02	52.14	10.57	2.70	13.25	73.7	0.694	0.001	0.1566	0.004	0.1330	0.027	0.0069	0.034
JR_D_z03	40.55	4.82	0.00	0.00	79.8	1.886	0.003	0.3936	0.009	0.2272	0.027	0.0000	0.000
JR_J_z01	33.10	2.30	0.55	1.43	79.2	4.173	0.002	0.8550	0.015	0.3960	0.027	0.0066	0.017
JR_J_z02	44.39	3.15	1.23	2.99	193.8	5.148	0.010	1.5859	0.029	0.3839	0.027	0.0106	0.026
JR_J_z03	39.25	3.45	0.00	0.00	74.4	2.009	0.002	0.5094	0.009	0.3070	0.027	0.0000	0.000
JR_K_z01	53.77	2.06	0.00	0.00	179.7	9.062	0.008	2.3455	0.042	0.7549	0.029	0.0000	0.000
JR_K_z02	26.71	5.86	0.00	0.00	65.9	1.040	0.002	0.2742	0.006	0.1228	0.027	0.0000	0.000
JR_K_z03	21.61	4.35	0.00	0.00	237.4	4.733	0.005	1.4414	0.025	0.1341	0.027	0.0000	0.000
JR_O_z01	49.90	2.71	1.04	3.61	107.3	3.173	0.002	0.9652	0.017	0.5040	0.027	0.0105	0.036
JR_O_z02	48.50	3.32	0.00	0.00	107.3	2.487	0.002	0.7978	0.017	0.4037	0.028	0.0000	0.000
JR_O_z03	113.69	5.88	2.58	9.90	170.5	1.897	0.003	0.6700	0.012	0.5298	0.027	0.0120	0.046
JR_S_z01	19.07	2.97	0.00	0.00	47.3	1.775	0.002	0.3887	0.008	0.1729	0.027	0.0000	0.000
JR_S_z02	76.37	2.89	5.04	7.43	94.7	3.773	0.004	0.7356	0.013	0.7323	0.028	0.0483	0.071
JR_S_z03	33.68	3.50	4.48	9.85	91.0	2.630	0.003	0.6418	0.012	0.2602	0.027	0.0346	0.076
JR_S_z04	30.20	3.46	0.00	0.00	92.8	2.741	0.001	0.6734	0.012	0.2373	0.027	0.0000	0.000

Table 1. Full data table used for analysis in this study. See Appendix B for explanation.

Full Sample Name	Th/U	RawDate It (Ma)	±	Ft	± (%)	Corrected Date (It) (Ma)	Full Unc. (Ma)	Analytic Unc. (Ma)	Full Sample Name	Notes
JR_3_z02	0.69	47.70	0.76	0.80	7.0	59.809	4.227	0.7584	JR_3_z02	elongate and rounded, no pointy ends, like a cylander but rounded on the end
JR_3_z03	0.63	48.79	0.96	0.79	7.0	61.573	4.437	0.9590	JR_3_z03	ellipsoidal, inclusions, rounded
JR_5_z01	0.28	57.68	1.83	0.81	7.0	71.023	5.491	1.8339	JR_5_z01	med grain, rounded, some incs
JR_5_z02	0.17	30.26	0.49	0.82	7.0	36.938	2.671	0.4949	JR_5_z02	some inc, nice crystal form, aesymetric tips, one end slightly rounded
JR_5_z03	0.11	17.73	0.29	0.84	7.0	21.183	1.532	0.2864	JR_5_z03	symetric grain, rounded, some incs
JR_A_z01	0.11	32.21	0.64	0.73	7.0	44.359	3.229	0.6383	JR_A_z01	best crystal form, rounded ends, clear and glassy
JR_A_z03	0.26	32.71	0.56	0.76	7.0	42.762	3.085	0.5579	JR_A_z03	rounded, symmetric, inclusions, not as clear
JR_D_z01	0.08	18.10	0.34	0.79	7.0	22.875	1.648	0.3404	JR_D_z01	nice crystal form, inclusions, slightly rounded
JR_D_z02	0.85	30.45	1.25	0.75	7.0	40.430	3.207	1.2453	JR_D_z02	rounded, symmetric, inclusions, not as clear
JR_D_z03	0.58	34.80	0.86	0.80	7.0	43.208	3.163	0.8637	JR_D_z03	rounded, darker
JR_J_z01	0.46	36.31	0.61	0.83	7.0	43.760	3.168	0.6053	JR_J_z01	aesymetric grain, some inc, possibly fractured tip
JR_J_z02	0.24	25.37	0.43	0.81	7.0	31.207	2.264	0.4339	JR_J_z02	symetric grain, nice crystal form, some incs
JR_J_z03	0.60	28.52	0.53	0.81	7.0	35.358	2.575	0.5331	JR_J_z03	symetric grain, nice crystal form, some incs
JR_K_z01	0.32	29.66	0.49	0.85	7.0	34.681	2.481	0.4885	JR_K_z01	inclusions, rounded
JR_K_z02	0.45	28.35	0.80	0.79	7.0	35.730	2.658	0.7965	JR_K_z02	inclusions, very well rounded, no sharp points, but not ellipsoidal
JR_K_z03	0.09	26.55	0.45	0.81	7.0	32.591	2.313	0.4497	JR_K_z03	good crystal form, but rounded ends
JR_O_z01	0.52	24.18	0.40	0.85	7.0	28.493	2.044	0.3995	JR_O_z01	almost spherical, pretty rounded
JR_O_z02	0.51	23.01	0.46	0.83	7.0	27.765	2.006	0.4569	JR_O_z02	rounded, inclusions
JR_O_z03	0.79	19.72	0.33	0.80	7.0	24.780	1.766	0.3332	JR_O_z03	rounded, one pointy end, inclusions
JR_S_z01	0.44	34.12	0.79	0.84	7.0	40.377	2.973	0.7934	JR_S_z01	ellipsoidal, clear
JR_S_z02	1.00	34.26	0.54	0.85	7.0	40.456	2.895	0.5444	JR_S_z02	ellipsoidal, not as clean as 1
JR_S_z03	0.41	30.88	0.60	0.84	7.0	36.873	2.668	0.5952	JR_S_z03	ellipsoidal, no clear inclusions
JR_S_z04	0.35	31.04	0.56	0.84	7.0	36.957	2.668	0.5573	JR_S_z04	ellipsoidal, no clear inclusions

APPENDIX B – METHODS & DATA EXPLANATION

"Generic Methods" of (U-Th)/He Analysis Performed in Tectonics and Thermochronometry Lab at the University of Colorado-Boulder via Dr. James Metcalf

Individual mineral grains are handpicked using a Leica M165 binocular microscope equipped with a calibrated digital camera and capable of both reflected and transmitted, polarized light. The grains are screened for quality, including crystal size, shape, and the presence of inclusions. After characterization, grains are placed into small Nb tubes that are then crimped on both ends. This Nb packet is then loaded into an ASI Alphachron He extraction and measurement line. The packet is placed in the UHV extraction line (~3 X 10^{-8} torr) and heated with a diode laser to ~800-1100°C for 5 to 10 minutes to extract the radiogenic ^{4}He. The degassed ^{4}He is then spiked with approximately 13 ncc of pure ^{3}He, cleaned via interaction with two SAES getters, and analyzed on a Balzers PrismaPlus QME 220 quadrupole mass spectrometer. Degassed grains are then removed from the line, and taken to a Class 10 clean lab for dissolution. Apatite grains, still enclosed in the Nb tubes, are placed in 1.5 mL Cetac vials, spiked with a ^{235}U - ^{230}Th tracer in HNO_3, capped, and baked in a lab oven at 80°C for 2 hours. Zircon, titanite, and other more refractory phases are dissolved using Parr large-capacity dissolution vessels in a multi-step acid-vapor dissolution process. Grains (including the Nb tube) are placed in Ludwig-style Savillex vials, spiked with a ^{235}U - ^{230}Th tracer, and mixed with 200 µl of Optima grade HF. The vials are then capped, stacked in a 125 mL Teflon liner, placed in a Parr dissolution vessel, and baked at 220°C for 72 hours. After cooling, the vials are uncapped and dried down on a 90°C hot plate until dry. The vials then undergo a second round of acid-

vapor dissolution, this time with 200 µl of Optima grade HCl in each vial that is baked at 200°C for 24 hours. Vials are then dried down a second time on a hot plate. Once dry, 200 µl of a 7:1 HNO_3:HF mixture is added to each vial, the vial is capped, and cooked on the hot plate at 90°C for 4 hours. Once the minerals are dissolved, regardless of the dissolution process, they are diluted with 1 to 3 mL of doubly-deionized water, and taken to the ICP-MS lab for analysis. Sample solutions, along with standards and blanks, are analyzed for U, Th, and Sm content using a Thermo Element 2 magnetic sector mass spectrometer. Once the U, Th, and Sm contents have been measured, He dates and all associated data are calculated on a custom spreadsheet made by CU TRaIL staff.

(U-Th)/He Data Explanation via Dr. James Metcalf (Tectonics and Thermochronometry Lab at the University of Colorado-Boulder)

Full Sample Name – Sample Name, the subscripts _z1 refer to separate analyses from the same sample

length and width – measurements of the grain dimensions in micrometers. Each grain is measured from two different angles to ensure that the grain geometry is fully captured.

2X Term – Notes whether or not the grain is doubly terminated. Grains that are broken re corrected for length following the technique of Farley (2002).

Dim Mass – The dimensional mass (in micrograms) is calculated based solely on the volume of the crystal (determined from the measurements) and average apatite density.

rs – The radius of a sphere with an equivalent surface are to volume ratio as your crystal. This value is required if you wish to do any thermal modeling of your grains using HeFTy.

4He (nmol/g) – the amount of 4He measured in the crystal via isotope dilution. This includes all of the He if multiple degassing steps were required. The ± column is 1-sigma analytical uncertainty.

U (ppm) – the amount of total U in the sample, measured via isotope dilution on an ICP-MS. The ± column is 1-sigma analytical uncertainty. A value of 0.00 indicates measurements that are not larger than analytical uncertainty.

Th (ppm) – the amount of total Th in the sample, measured via isotope dilution on an ICP-MS. The ± column is 1-sigma analytical uncertainty. A value of 0.00 indicates measurements that are not larger than analytical uncertainty.

Sm (ppm) – the amount of total Sm in the sample, measured via isotope dilution on an ICP-MS. The ± column is 1-sigma analytical uncertainty. A value of 0.00 indicates measurements that are not larger than analytical uncertainty.

eU – the effective Uranium, a measurement of the total amount of radiation experienced by the crystal, equivalent to U + .235Th.

Raw Date (Ma) – the age calculated directly from He, U, Th, and Sm measurements. The ± column is 1-sigma analytical uncertainty.

Ft – The alpha ejection correction calculated using the method of Farley (2002). 1-Ft is a measure of the amount of He that was ejected from the crystal. An Ft of 1.00 would indicate that no He had been lost. This is a purely geometric correction. The ± column is 1-sigma uncertainty on the alpha ejection correction, and is estimated based on the size of the crystal, using the method of Ehlers and Farley, (2003).

Corrected Date (Ma) – The alpha-ejection corrected age, equal to the Raw Age divided by the alpha-ejection correction.

Full Unc (Ma) – The uncertainty in millions of years including the estimate for the uncertainty in the alpha ejection correction.

Analytic. Unc (Ma) – Uncertainty in millions of years not including the estimate for the uncertainty in the alpha ejection correction, and only including direct analytical uncertainties.

Notes – These are notes taken during the picking process. They often relate to the size, shape, and quality of the grains. Again, these can be helpful when identifying odd ages.

The sheet will also include results for the Fish Canyon Tuff standard zircons run in conjunction with your samples. These grains are degassed and dissolved alongside your samples, and have an

approximate age of 28.2 Ma, although in practice dates of 27.8 to 28.5 Ma are used. For more information, please see the following reference:

Rivera, T.A., Storey, M., Zeeden, C., Hilgen, F.J., and Kuiper, K., 2011, A refined astronomically calibrated 40Ar/39Ar age for Fish Canyon sanidine: Earth and Planetary Science Letters, v. 311, no. 3-4, p. 420–426, doi: doi:10.1016/j.epsl.2011.09.017.